J. Fluid Mech. (2005), *vol.* 533, *pp.* 125–159. © 2005 Cambridge University Press
doi:10.1017/S0022112005004325 Printed in the United Kingdom

Elliptic instability of a co-rotating vortex pair

By PATRICE MEUNIER AND THOMAS LEWEKE

Institut de Recherche sur les Phénomènes Hors Équilibre (IRPHE), CNRS/Universités Aix-Marseille I & II, 49 rue F. Joliot-Curie, B.P. 146, F-13384 Marseille Cedex 13, France

(Received 10 February 2004 and in revised form 18 January 2005)

In this paper, we report experimental results concerning a three-dimensional short-wave instability observed in a pair of equal co-rotating vortices. The pair is generated in water by impulsively started plates, and is analysed through dye visualizations and detailed quantitative measurements using particle image velocimetry. The instability mode, which is found to be stationary in the rotating frame of reference of the two-vortex system, consists of internal deformations of the vortex cores, which are characteristic of the elliptic instability occurring in strained vortical flows. Measurements of the spatial structure, wavelengths and growth rates are presented, as functions of Reynolds number and non-dimensional core size. The self-induced rotation of the vortex pair, which is not a background rotation of the entire flow, is found to lead to a shift of the unstable wavelength band to higher values, as well as to higher growth rates. In addition, a dramatic increase in the width of the unstable bands for large values of the rescaled core radius is found. Comparisons with recent theoretical results by Le Dizès & Laporte (2002) concerning elliptic instability of co-rotating vortices show very good agreement.

At later stages of the flow, when the perturbation amplitude becomes sufficiently large, the two vortices merge into a single structure. This happens for smaller cores sizes than in the case of two-dimensional merging. The three-dimensional merging leads to a final vortex characterized by turbulent small-scale motion, whose size appears to be larger than it would have been without instability. The vorticity profile of the final vortex is non-Gaussian after both two-dimensional and three-dimensional merging. The profile contains more vorticity outside the inner core than a Gaussian vortex, resulting from the ejection of vorticity filaments during the merging stage.

1. Introduction

The flow consisting of two parallel vortices having the same sense of rotation is one of the simplest configurations for the study of basic vortex interactions. In addition to its intrinsic interest on a fundamental level, it has relevance to a number of different flows and applications.

Co-rotating vortices are found in mixing layers, as a result of the Kelvin–Helmholtz instability. The merging of the vortices dictates the growth of the layer thickness, and the onset of three-dimensionality in the mixing layers could be linked to the appearance of an elliptic instability of these vortices (Bayly, Orszag & Herbert 1988). Vortex merging is also a major ingredient in the dynamics of two-dimensional turbulent flows, which motivated numerous studies on co-rotating vortices. In three-dimensional turbulence, many types of vortex interaction occur between the coherent structures discovered in these flows (Vincent & Meneguzzi 1991; Kida & Ohkitani 1992; Cadot, Douady & Couder 1995), including those between (almost) parallel

co-rotating vortices. Precise knowledge about their behaviour may lead to a deeper understanding of the complex global dynamics and scalings. Finally, on a more practical side, strong co-rotating vortices are found in the wake of many types of aircraft wings in landing configuration, i.e. with lowered flaps. They eventually merge into a single vortex behind each wing (Chen, Jacob & Savas 1999; Devenport, Vogel & Zsoldos 1999), which, owing to its strength and longevity, represents a danger for following aircraft, in particular in the vicinity of airports. Since this hazard, and the associated rules for separation distances, are the main factors limiting airport capacities today, a detailed analysis of the initial co-rotating vortex flow is of great interest in this context.

The two-dimensional evolution of two co-rotating vortices has been extensively studied numerically (see, e.g. Roberts & Christiansen 1972; Overman & Zabusky 1982). It appears that when the core size of the vortices is small compared to their separation distance, they rotate around each other almost like two point vortices. When the core size, which grows by viscous diffusion, reaches a critical fraction of the separation distance, two filaments of vorticity are ejected radially and the vortices approach each other to preserve the total angular momentum. As shown numerically (Overman & Zabusky 1982) and experimentally (Griffiths & Hopfinger 1987), they finally merge into a single vortex, which becomes axisymmetric by rolling up the filaments of vorticity into tight spirals (Melander & McWilliams 1987). Several numerical (Saffman & Szeto 1980; Dritschel 1985, 1986) and theoretical (Melander, Zabusky & McWilliams 1988) studies calculated the critical ratio of core size and separation distance, at which merging initiates, for patches of uniform vorticity. This criterion was generalized by Meunier *et al.* (2002) to the case of non-uniform distributions of vorticity, by defining the core size, not through the vortex area, but using the angular momentum and the circulation. A global theory based on the angular momentum of the filaments of vorticity ejected during the merging stage was proposed by Meunier (2001) and confirmed experimentally by Cerretelli & Williamson (2003). In all these analyses, the possibility of a three-dimensional instability, which could possibly modify this picture considerably, has not been considered.

Several three-dimensional instabilities occurring in systems of parallel vortices are known, in particular for the case of a counter-rotating pair. The first stability analysis of such a pair was performed by Crow (1970) on a counter-rotating vortex pair, to explain the observation of periodic symmetric perturbations of aircraft wakes. The growth of these perturbations is caused by the combined action of three effects: the strain field induced by each vortex at the location of the other one, the self-induced rotation of each perturbed vortex, and the flow field induced by the perturbations of the other vortex. Crow's analysis, in which the vortices were treated as lines, showed that all effects induce a rotation of a given wavy perturbation, and that they can cancel each other under certain conditions, producing a stationary wave which is pulled apart exponentially by the strain. This happens typically for wavelengths between 5 and 10 times the vortex separation distance. Using the same procedure, Jiménez (1975) proved that, for the case of co-rotating vortices, the different rotation rates could never add up to zero, which means that such flows are stable with respect to this instability mechanism. In the present study, we did indeed not observe any long-wavelength instability, which is consistent with this result.

In these previous analyses, the hypothesis of vortex filaments restricted the validity of the results to wavelengths much larger than the core size of the vortices. In order to extend the stability theory to smaller wavelengths, Moore & Saffman (1975) and Tsai & Widnall (1976) studied the stability of a finite-core vortex in a uniform stationary

straining field, which leads to locally elliptic streamlines. Their global analysis showed that neutral modes of the unstrained vortex (Kelvin modes) could be resonantly amplified by the strain, leading to short-wave instability.

The elliptic instability was rediscovered from a local viewpoint, i.e. assuming the wavelength is small compared to the size of the region with elliptic flow (core size). Pierrehumbert (1986) and Bayly (1986) studied the three-dimensional stability of an inviscid elliptic flow of infinite extent, showing that inertial waves, found in rotating flows (Greenspan 1968), could be amplified parametrically by the strain, leading to instability. Landman & Saffman (1987), following the analysis of Craik & Criminale (1986), extended this result to include viscous effects. This work has been generalized by Lifschitz & Hameiri (1991) to the case where inertial waves cannot be calculated analytically, by using the methods of 'geometric optics'. The case of a rotating elliptic flow was studied by Craik (1989), Leblanc (1997), Leblanc & Cambon (1998), and Le Dizès (2000*b*). Waleffe (1990) showed that combinations of unstable inertial waves can lead to localized disturbances, which can satisfy certain boundary conditions, e.g. for flow in cylindrical containers. Moreover, the structure of this disturbance is comparable to the inner profile of the Kelvin waves of the global analysis cited above, proving that the two approaches describe the same phenomenon. A comprehensive review of elliptic instability has been given by Kerswell (2002).

Experimental results on three-dimensional instabilities of a vortex pair are very rare, and treat mostly the counter-rotating case. Short-wave instabilities were initially observed on vortex rings by Krutzsch (1939), Maxworthy (1972) and Widnall & Sullivan (1973). Thomas & Auerbach (1994) found such an instability on a counter-rotating vortex pair, which showed a certain resemblance with the theory of Tsai & Widnall (1976). A more detailed study of the counter-rotating vortex pair was made by Leweke & Williamson (1998), showing that the instability has the same structure as the perturbation found by Waleffe (1990), and that wavelengths and growth rates are in agreement with the two preceding theories. Experiments dedicated more specifically to the elliptic instability were performed by Vladimirov, Makarenko & Tarasov (1987), Malkus (1989) and Eloy, Le Gal & Le Dizès (2000), who studied flows inside an elliptical container, showing good agreement with the theory of Waleffe (1990). In all these studies, the strain felt by a given vortex was stationary. So far no experimental result is available on the effect of a time-dependent, and in particular a rotating strain. In the present study, we investigate experimentally the short-wavelength instability of a symmetric laminar co-rotating vortex pair, which is the simplest configuration in which a vortex experiences a rotating strain. Some preliminary results of this work concerning the existence of the elliptic instability in this flow were reported by Meunier & Leweke (2001), and are presented again in figures 6, 11(*b*), 12(*a*) and 26 for clarity. Moreover, the dye visualizations of figures 9(*b*), 10(*b*), 22(*b*) and 23 have been published in the Gallery of Fluid Motion (Meunier & Leweke 2000). In this paper, we give a detailed qualitative and quantitative description of the phenomenon.

After a description of the experimental apparatus and the two-dimensional base flow in § 2, we show in § 3 the overall structure and symmetry of the instability in our flow. In § 4, we present measurements of wavelengths and growth rates as a function of the parameters of the flow, and make comparisons with theoretical results on elliptic instability, in particular with those from Le Dizès & Laporte (2002), which directly treats the flow considered here. Section 5 shows how the instability modifies the merging process of the two vortices, which occurs at late stages, with respect to the purely two-dimensional case. Conclusions follow in § 6.

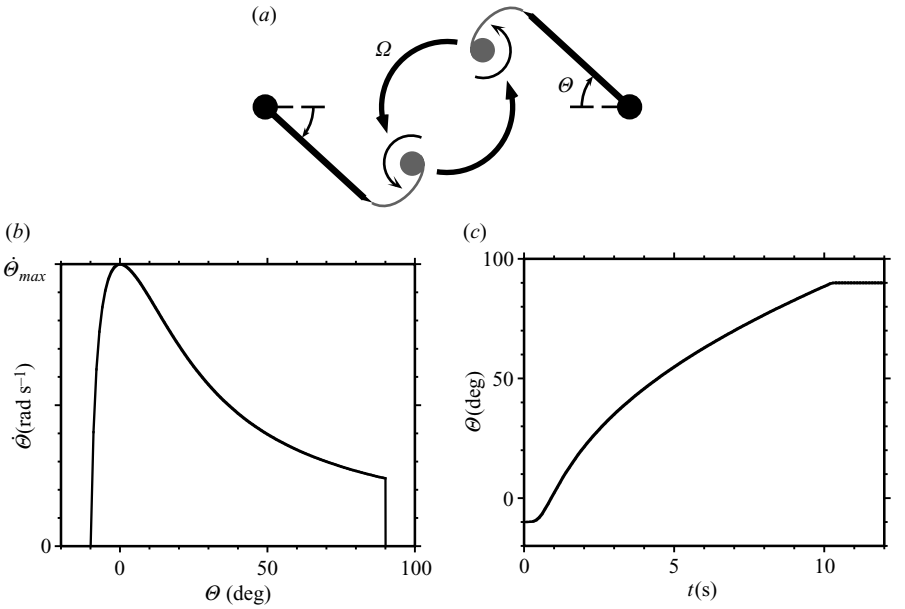


FIGURE 1. Generation of the vortices. (*a*) Principle of the experimental set-up. (*b*) Variation of the angular velocity $\dot{\Theta}$ of the generating plates as function of their angle Θ, for a movement defined by (2.1). (*c*) Time evolution of the angle Θ of the plates, for a maximal angular velocity $\dot{\Theta}_{max} = 0.4$ rad s^{-1}.

2. Experimental details and base flow

2.1. *Set-up and methods*

The flow was studied in a rectangular water container with Plexiglas walls, having a square base of 56×56 cm^2 and a height of 133 cm. Two vertical vortices are created using two flat plates, impulsively rotated from rest around their vertical edges, as shown schematically in figure 1(*a*). The two resulting starting vortices rotate around each other by mutual induction. An example of a cross-cut visualization of the initial pair is shown in figure 2. The plates are anodized for protection against oxidation, and painted in black for a good contrast in the flow visualization. They have dimensions $135 \times 10 \times 0.5$ cm^3 and their free edges are sharpened to an angle of 30°. The high aspect ratio of the plates creates long and thin vortices; this is required to keep the effects of axial velocity, induced by the end conditions at the bottom of the tank, away from the observation area, consisting of the upper 40 cm below the free surface. The plates are driven by computer-controlled step-motors. A high reduction in the gears leads to a displacement $\Delta\Theta = 0.0225°$/step of the plates, giving them a smooth movement. The separation between the two tips of the plates is 3.2 cm when the plates are aligned, i.e. for an angle $\Theta = 0$ (see figure 1*a*). The plates start from a negative angle $\Theta = -10°$, so that the vortices are fully created before they begin to interact.

The motion history of the plates has been chosen carefully, through empirical improvements, to avoid instabilities during the roll-up process, and create concentrated vortices which follow an approximately circular path, despite the presence of the plates. The motion profile (angular velocity as function of angle) that was finally adopted is:

$$\dot{\Theta} = \dot{\Theta}_{max} \frac{23°}{\Theta + 11°} \left\{ 1 - \mathrm{e}^{-((\Theta+10°)/15°)^{5/4}} \right\}. \tag{2.1}$$

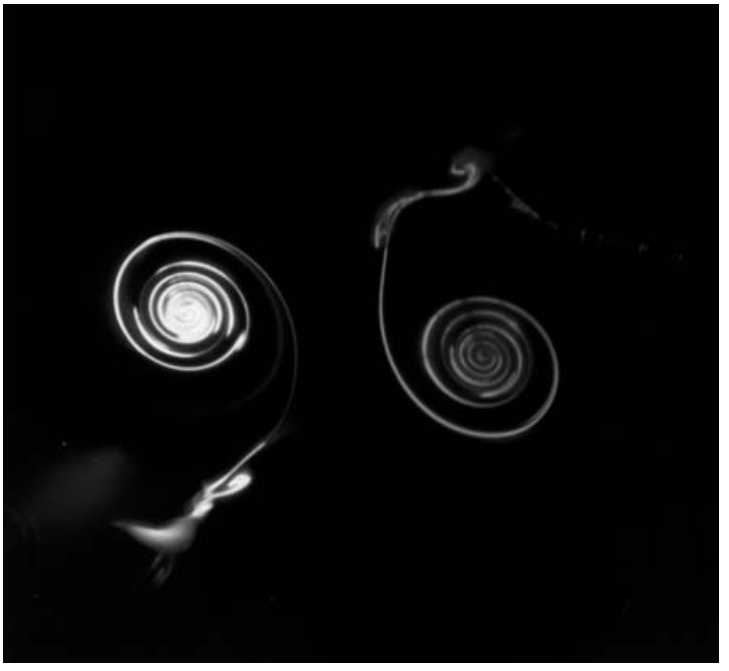


FIGURE 2. Dye visualization of the co-rotating vortex pair in a plane perpendicular to their axes. The right generating plate is faintly visible; it ends at the beginning of the right dye filament.

It is plotted in figure 1(*b*), and consists of a strong but smooth acceleration, followed by a gradual slowing-down. They stop when they reach $\Theta = 90°$, as shown in figure 1(*c*). The maximum angular velocity $\dot{\Theta}_{max}$ is varied between 0.1 and 0.4 rad s^{-1} to adjust the circulation of the vortices, which defines the Reynolds number (see below). A possible difference in the circulations of the two vortices, coming from residual convection motion in the tank, is corrected for each experiment by adjusting $\dot{\Theta}_{max}$ for each vortex individually.

In order to visualize the flow, two fluorescent dyes (fluorescein and rhodamine B) are painted along the edges of the plates. For this purpose, the plates, whose supports are mounted on a carriage on vertical rails, can be lifted out of the water before the experiment. When the dyes are dry, the plates are then lowered slowly into the water without disturbing the fluid significantly. During the rotating motion of the plates, the dye washes off the plates and very effectively marks the vortex centres, as seen in figure 2. The flow is illuminated with light from a 5 W argon laser, either in volume or in a horizontal plane perpendicular to the vortex axes. Images are recorded either on video tape, a computer using a digital high-resolution camera, or on a standard 35 mm photographic film.

Quantitative measurements of velocity fields are obtained by digital particle image velocimetry (DPIV). For this method, the flow is seeded with small reflecting particles of mean diameter 50 μm and density 1.00 ± 0.02 g cm^{-3}, illuminated by a sheet of laser light of 3–5 mm thickness. These particles can be expected to follow the laminar motion of the fluid correctly, since the characteristic length scales are of the order of the vortex core size, i.e. more than two orders of magnitude larger than the particle diameter. Image pairs are recorded by a high-resolution digital

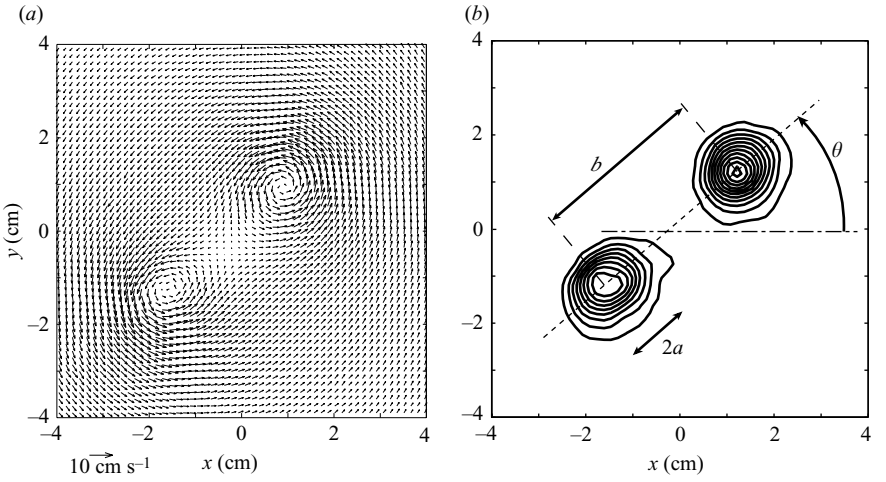


FIGURE 3. (*a*) Typical velocity field and (*b*) vorticity contours obtained by PIV measurements for a core size-to-separation distance ratio $a/b = 0.17$ and a $Re = 3600$. The difference between two vorticity contours is $2\,\mathrm{s}^{-1}$.

camera of 1008×1018 pixels, with a time delay of 33 ms when using a continuous argon laser, and 15 ms when using two pulsed Nd-YAG lasers for higher Reynolds numbers. The images are treated by a cross-correlation algorithm developed for velocity fields containing high velocity gradients. The interrogation windows, of dimensions 32×32 pixels (corresponding to about $3 \times 3\,\mathrm{mm}^2$), are translated and deformed according to the velocity gradients, to keep the correlation peaks as high as possible in the case of intense velocity gradients (Meunier & Leweke 2003). One obtains a velocity field of 60×60 vectors, to which a median filter is applied, which corrects the spurious vectors (2 % on average). A typical initial velocity field is shown in figure 3(*a*), where no smoothing was applied. From these velocity fields, the axial vorticity can be calculated using finite-difference or contour methods (figure 3*b*).

2.2. *Characteristics of the two-dimensional base flow and their determination*

DPIV measurements are necessary to determine accurately the initial conditions of the flow, which for the present problem means the two-dimensional velocity field before the appearance of the three-dimensional instability. Precise knowledge of these conditions is essential for a meaningful comparison with theoretical results, since theoretical predictions are very dependent on the two-dimensional distribution of vorticity. A detailed study of the two-dimensional flow was presented in Meunier *et al.* (2002); here, we only recall the main results necessary for the present purpose.

A pair of equal co-rotating vortices is characterized by the circulation Γ of each vortex, the separation distance b between the two vortex centres, and their characteristic core radius a. These quantities were determined in the following way:

The circulation Γ is calculated by integrating the velocity on a streamline around each vortex. Its determination is very precise since the PIV velocity measurements are very accurate outside the vortex cores. The uncertainty in the circulation is found to be small: $\Delta\Gamma/\Gamma \approx 1\,\%$. The circulation of one vortex is used to define the Reynolds number of the flow: $Re = \Gamma/\nu$. It was varied between 1000 and 5000 for this study.

To define the core size of the vortices properly, we must examine their individual velocity distributions. From measurements as in figure 3, we determine the azimuthal

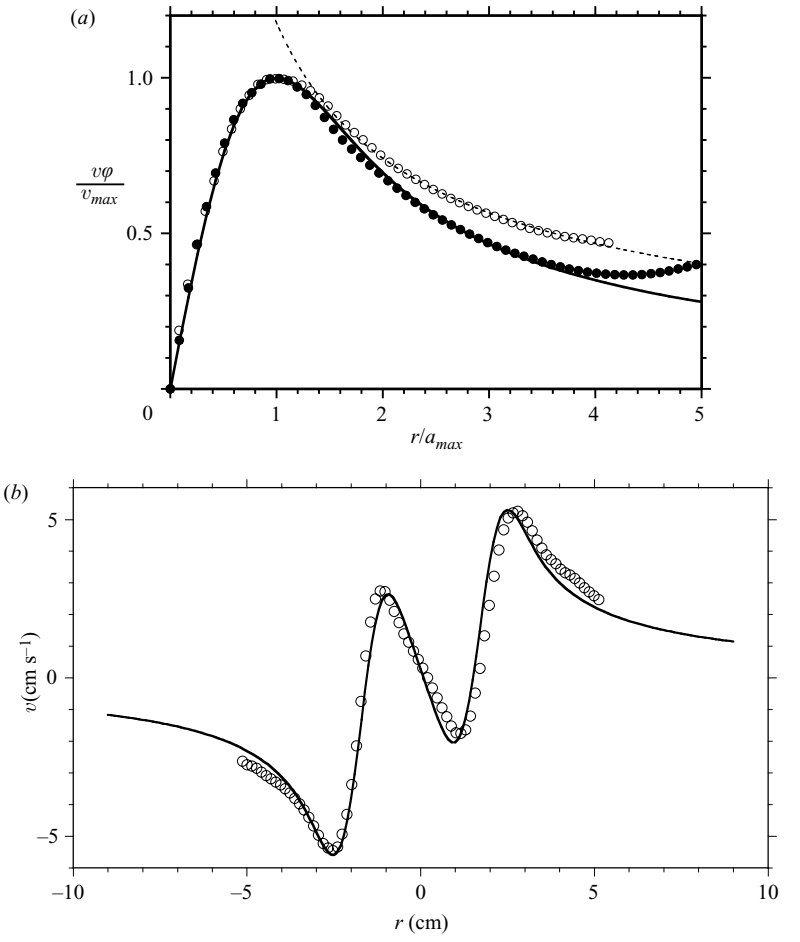


FIGURE 4. (*a*) Typical profile of the mean azimuthal velocity of one vortex for $Re = 1506$ (filled symbols) and for $Re = 3350$ (open symbols). (*b*) Transverse velocity profile on a line joining the two vortex centres for $Re = 3350$. The solid lines correspond to theoretical predictions obtained for Gaussian vortices defined by (2.2). The dashed line in (*a*) corresponds to a power law $v_\varphi \propto r^{-2/3}$.

velocity v_θ, as function of the radial distance r from the centre of a given vortex, i.e. the local maximum of vorticity. An example of the azimuthally averaged profile $v_\theta(r)$ is shown in figure 4(*a*). The radius a_{max} at which the mean azimuthal velocity is maximum is very well defined; it will be used for the definition of the core size a. The comparison in figure 4(*a*) with the profile of a Gaussian vortex, given by

$$v_\theta(r) = \frac{\Gamma}{2\pi r}\left(1 - \mathrm{e}^{-r^2/a^2}\right), \tag{2.2}$$

shows that the experimental vortex is very well represented by such a profile at small Reynolds numbers. For higher Reynolds numbers, the agreement is less good outside the core, but remains excellent inside the inner core. Fabre & Jacquin (2004) have shown theoretically that the characteristics of the elliptic instability are mainly determined by the profile of vorticity inside the core for the class of vortices encountered in the present study, and we expect the difference between the two

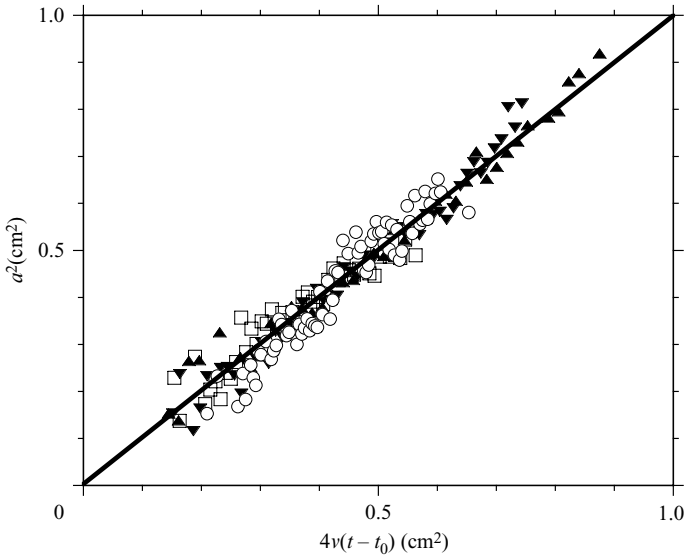


FIGURE 5. Time evolution of the square of the core size a for a co-rotating vortex pair with initial separation distance $b_0 \approx 3$ cm. The solid line corresponds to the theoretical prediction (2.3) with appropriate choices of t_0, obtained for a Gaussian vortex defined by (2.2). ▲, $Re = 742$; ▼, 1506; □, 2258; ○, 3600.

profiles to be negligible concerning the instability features, although the enlargement of the profile could lead to a slight underestimate of the core size a.

For a Gaussian vortex, the radius a_{max} of maximum circumferential velocity is related to the core parameter a in (2.2) by: $a \approx a_{max}/1.12$. In the following, we will use the same relation to calculate the core radius of the experimental vortices. We adopt this method, rather than a least-squares fit of the velocity field to the superposition of two Gaussian vortices, since it remains applicable for general vorticity profiles, in particular those found after the merging process, which are clearly not Gaussian any more. In figure 4(a), when the radius becomes of the order of the separation distance between vortices (for $r/a_{max} \gtrsim 4$), the experimental values are higher than those for a Gaussian vortex. This is probably caused by the presence of the second vortex, whose velocity field contributes to the measurements around the first. In figure 4(b), the second vortex was included in the comparison, which shows the velocity component perpendicular to the line joining the two vortices, as function of the position along this line. The agreement between measurement and the prediction using Gaussian vortices is very good.

The core size increases in time owing to viscous diffusion of vorticity. Measurements of this growth are shown in figure 5 for different experiments. They follow quite nicely the theoretical evolution for a Gaussian vortex, given by

$$a^2 = 4\nu(t - t_o). \tag{2.3}$$

Use of such a linear fit to a given set of data, allows the determination of a at a given time in the experiment with an uncertainty of $\Delta a/a \approx 4\,\%$, despite the scatter observed in figure 5.

The separation distance b between the two vortex centres is found from the location of the two local vorticity maxima, measured on smoothed vorticity fields. The effect of one vortex on the location of the other maximum is negligible, even when the

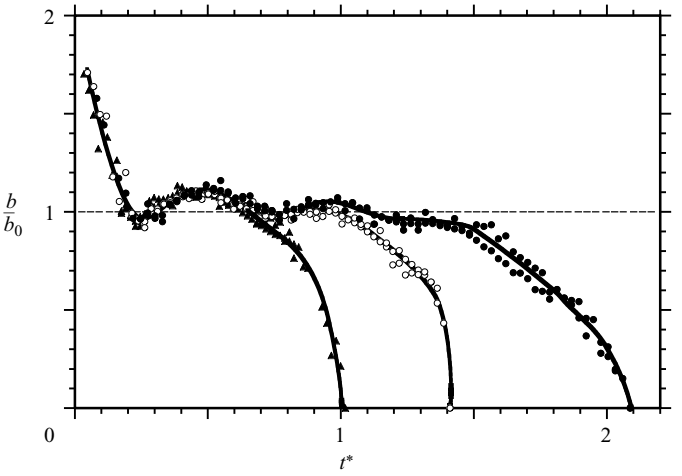


FIGURE 6. Evolution of the separation distance b between the two vortex centres with non-dimensional time $t^* = t/t_c$ for three different Reynolds numbers. ▲, $Re = 742$; ○, 1506; ●, 2258.

vortices are very close. Considering again nearly Gaussian vortices, and the worst case of $a/b \approx 0.25$ (for higher values, the vortices merge), the vorticity of the first vortex is 10^{-7} times the vorticity of the second vortex at the centre of the latter. The error in the measurement of the separation distance is therefore relatively small $\Delta b/b \approx 2\,\%$. Figure 6 shows the evolution of the separation distance b as function of the non-dimensional time t^* (see equation (2.5)). The origin of time is taken at the beginning of the plate motion. After an initial phase of vortex formation ($t^* < 0.2$), the separation distance remains fairly constant, although slight oscillations are visible, owing to the presence of the vortex-generating plates in our set-up. The average value during this second phase defines the 'initial' separation distance b_0, which is used to non-dimensionalize distances in the experiment, and in particular the core size a (Meunier & Leweke 2001).

In this stage, the vortices rotate around each other. The orientation θ of the pair (see figure 3), which is also obtained from the locations of vorticity maxima, is plotted in figure 7 as a function of time. It increases almost linearly with a mean angular velocity close to the angular velocity Ω of a system of two point vortices with the same circulation and separation distance:

$$\Omega = \frac{\Gamma}{\pi b_0^2}. \tag{2.4}$$

Some slight variations of the angular velocity can be observed in the measurements, which are due to the variations of the separation distance, as seen above. Indeed, when taking into account the instantaneous separation distance measure in the same experiment, the agreement between measurement and point-vortex prediction is much better (see figure 7).

The average period of rotation of the pair

$$t_c = \frac{2\pi^2 b_0^2}{\Gamma} \tag{2.5}$$

is used to non-dimensionalize time t: $t^* = t/t_c$.

As explained by Meunier *et al.* (2002), when the core size a reaches approximately 25 % of the separation distance b, a rapid change in the two-dimensional flow occurs.

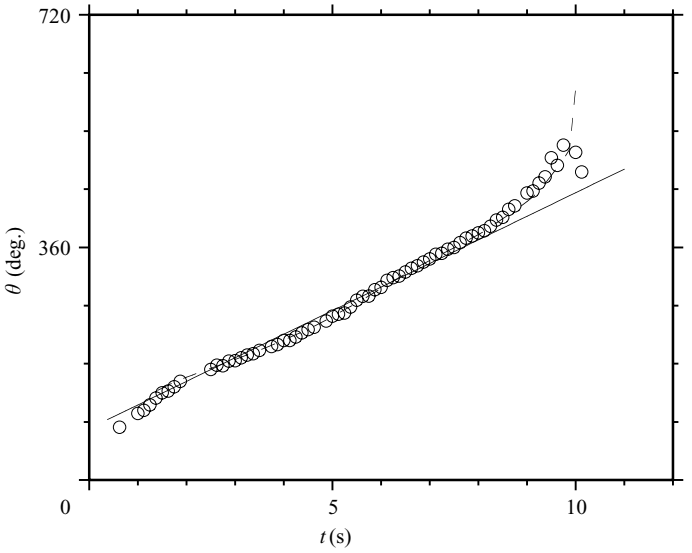


FIGURE 7. Time evolution of the angle θ of the vortex pair for $Re = 3600$. The lines correspond to the orientation of two point vortices of the same circulation, separated by a constant averaged distance $b = 4$ cm (solid line), or by a time-varying distance $b(t)$ (dashed line) obtained in the same experiment.

The vortex separation distance starts to decrease quickly (figure 6), and the two vortices merge into a single final one in a mainly convective process. For low Reynolds numbers, the flow is found to remain two-dimensional throughout. The instability developing in the initial vortex pair at higher speeds leads to three-dimensional unstable merging, which is treated in § 5 below.

2.3. *Measurements of the three-dimensional flow*

As shown in the following sections, a three-dimensional instability appears in the co-rotating vortex flow, when the Reynolds number is sufficiently high. It is characterized by internal deformations of the vortex cores, which are antisymmetric with respect to the centre of rotation of the pair. In the unforced natural case, the wavelength of the perturbations was somewhat varying along the vortex, and its phase was random for a given run. A special procedure had to be adopted, in order to obtain the quantitative results presented in § 4.

For most visualizations and measurements presented in this paper, the flow was excited at a particular wavelength, close to the naturally occurring one. This control was achieved by sticking small pieces of adhesive tape (dimensions $5 \times 9\,\mathrm{mm}^2$) close to (but not exceeding) the edge of the generating plates, separated by the desired wavelength (typically 3–4 cm). This very small perturbation was sufficient, in most cases, to fix the wavelength and phase of the developing instability. In this way, the three-dimensional flow was much more regular, and quantitative measurements became possible. The wavelength and phase were nevertheless checked in each run from side-view visualizations.

The fact that the phase of the three-dimensional perturbations was fixed made possible the measurements of the growth of the vortex centreline waviness, using dye and simultaneous visualization of two cross-cut planes, as described in § 3. (DPIV measurements are not precise enough to obtain this quantity with any reasonable degree of precision in this kind of flow.) It was verified (see § 4), using numerical simulations and analytical expressions of the perturbations that the growth rate

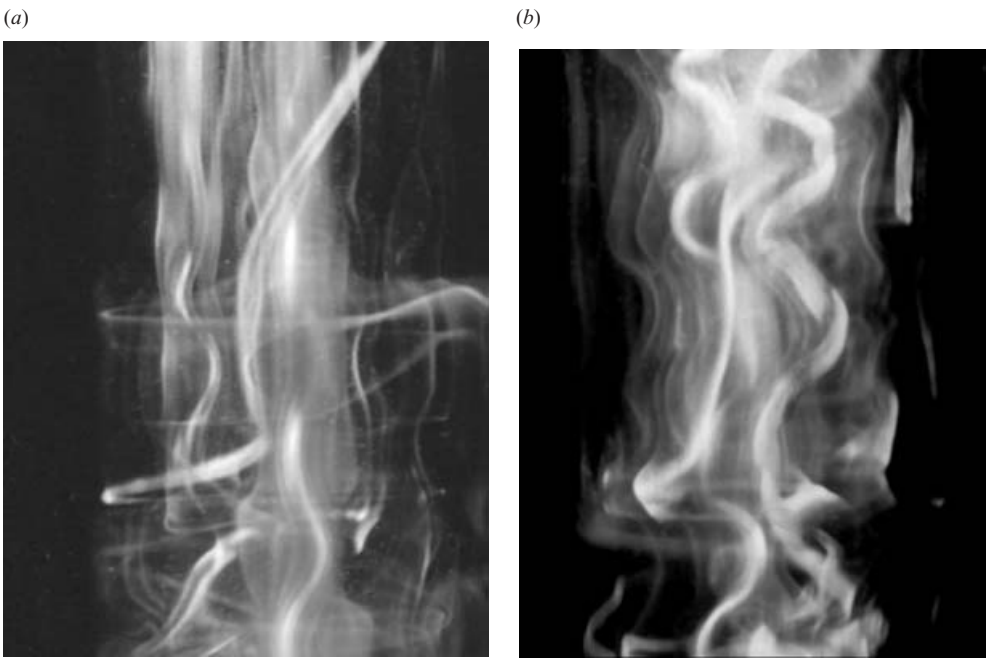


FIGURE 8. Side-view visualizations of the freely developing three-dimensional instability of a co-rotating vortex pair, for a Reynolds number of approximately 3000.

obtained in this way is identical to the growth rate of the unstable mode, provided that the amplitude of the dye wave is smaller than the core size a, for the case of a Gaussian vortex. The values of a and the vortex separation distance b, associated with a given measurement of growth rate, represent average values during the period in which the growth rate was determined, i.e. in which exponential growth was observed. Despite all these precautions, the uncertainty in the (dimensionless) growth rate must be estimated to be about 25 %, based on the observed scatter. This may be due to a number of effects, e.g. residual motion, in the tank, of random perturbations during vortex roll-up generating waves that travel along the vortices and shift the phase of the three-dimensional perturbations, inducing errors in the measurement of the amplitude. This illustrates the high sensitivity of the vortex flow studied here, and the difficulties of obtaining quantitative information.

Other quantities concerning the three-dimensional instability, in particular certain length scales related to the mode structure, were obtained from visualizations or DPIV measurements. The error estimates given below for these quantities reflect the precision with which they could be read off the images, using, where possible, averages over several wavelengths of the instability.

3. Three-dimensional instability of the vortex pair

At low Reynolds numbers, the flow remains laminar and two-dimensional. The two vortices merge before the onset of a three-dimensional perturbation; this has been analysed in great detail by Meunier *et al.* (2002). For high Reynolds numbers ($Re > 2000$), we observed the rapid emergence of a three-dimensional perturbation of the vortices at a relatively regular wavelength, without any excitation. Such instabilities are presented in the side-view visualizations of figure 8; they consist of wavy deformations of the centrelines of the vortices. In this section, we are going

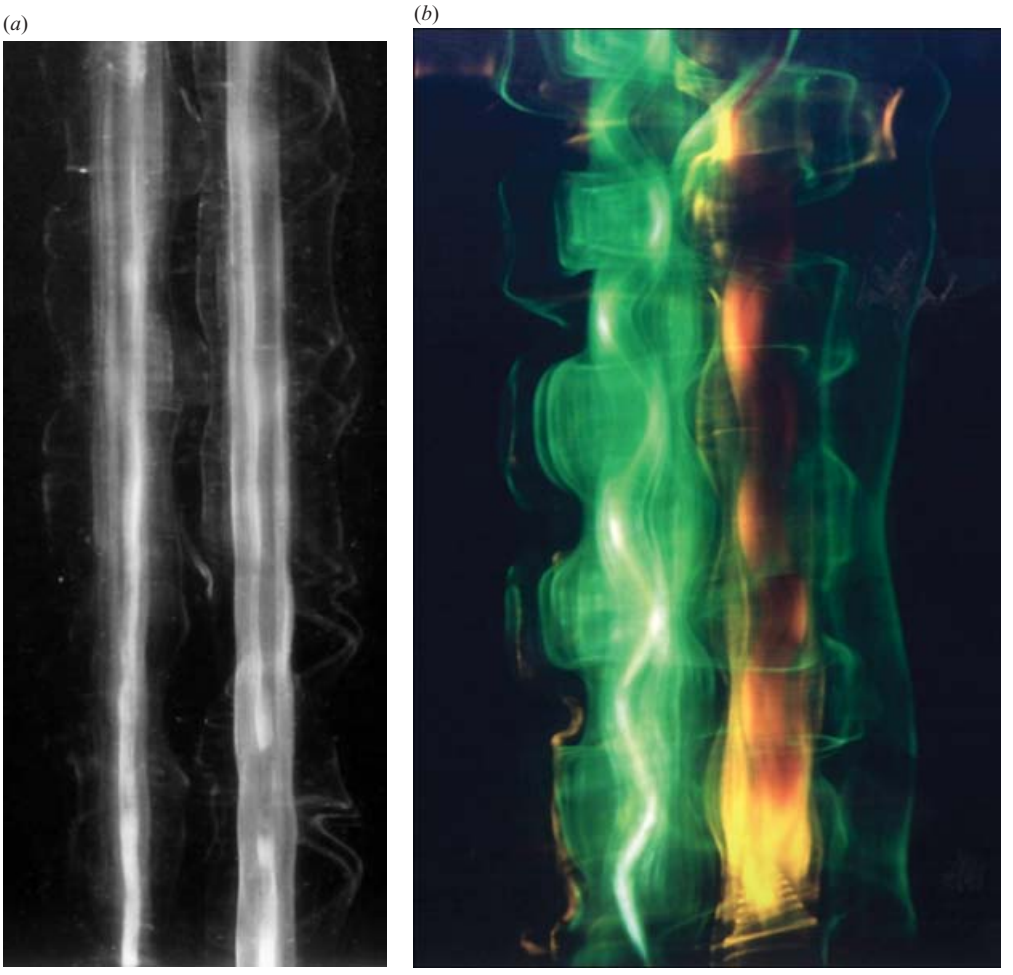


FIGURE 9. Orthogonal side views of the three-dimensional instability in a co-rotating vortex pair, for $Re \approx 3000$ and a wavelength $\lambda = 3.5$ cm. The vortices are in a plane oriented at (a) -45° and (b) $+45^\circ$ with respect to the paper. The perturbation is orthogonal to the plane of the paper and contained in the plane of the paper, respectively.

to describe the shape of this perturbation and give some quantitative characteristics of its structure, based on different visualizations. Although the instability has been first observed without excitation, it was then convenient to excite only one wavelength by placing small pieces of tape on the plates, in order to freeze the phase of the instability and make the observations more repeatable.

Figure 9(b) shows the shape of the instability at $t^* \approx 1.3$, consisting in a wavy perturbation of the two vortex centrelines in the plane of the image. The two centrelines are in phase, showing that the instability is antisymmetric with respect to the centre of the vortex pair. This symmetry has been observed in most cases, in the presence or in the absence of an excitation of the instability, and for a symmetric or antisymmetric excitation. The same antisymmetry was obtained for the elliptic instability of a counter-rotating vortex pair by Leweke & Williamson (1998) and was explained by the cooperation of the two instabilities at the centre of the vortex pair, through a matching condition of the two perturbations.

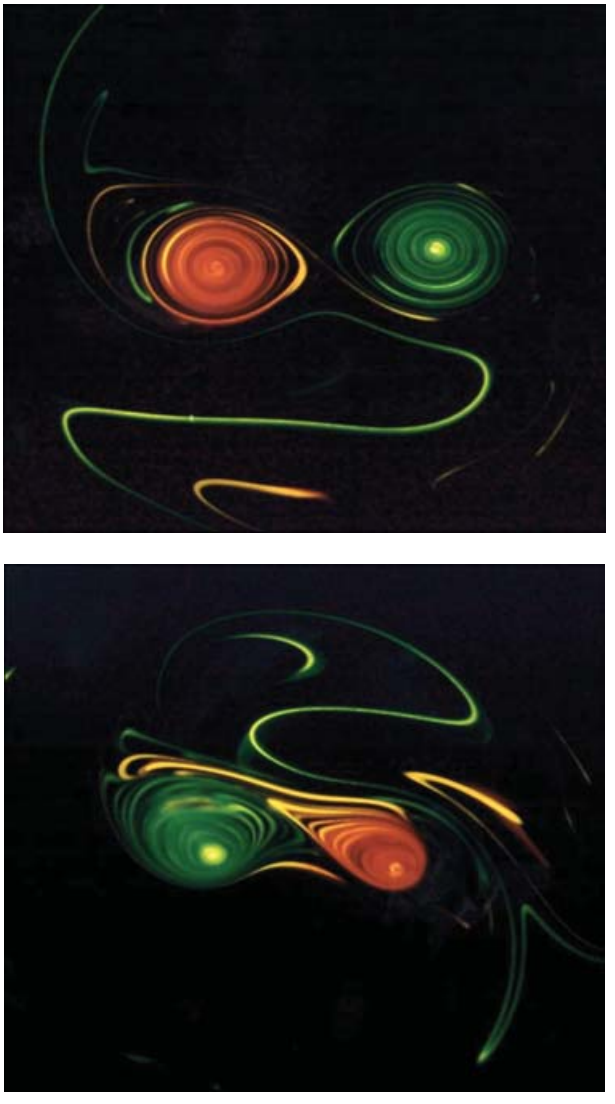


FIGURE 10. Cross-cut visualization of the three-dimensional instability, for a $Re \approx 3000$ and $\lambda = 3.5$ cm. (*a*) $t^* \approx 0.8$; (*b*) $t^* \approx 1.3$.

In figure 9(*b*), the two vortices are not in the plane of the figure: the upper vortex (resp. lower) is in front of (resp. behind) the plane of the figure. Figure 9(*a*) shows the pair one quarter period of rotation earlier (for $t^* \approx 1$), when the upper (resp. lower) vortex is behind (resp. in front of) the plane of the figure. For this particular orientation of the vortex pair, the undulation is not visible, although the perturbation is present (revealed by cross-cut visualizations), but it lies in a plane perpendicular to the plane of the figure. This proves that the centrelines are not located on a spiral, but on a plane, which is not aligned with the vortex pair. A proper determination of the angle of the plane of the perturbations will be made at the end of this section.

Figure 10(*b*) shows a cross-cut view of the instability on a plane perpendicular to the axes of the vortices (section *C*–*C* in figure 11*a*), at a maximum of the perturbation. The instability breaks the initial symmetry of the pair (visible in figure 10*a*). The effect

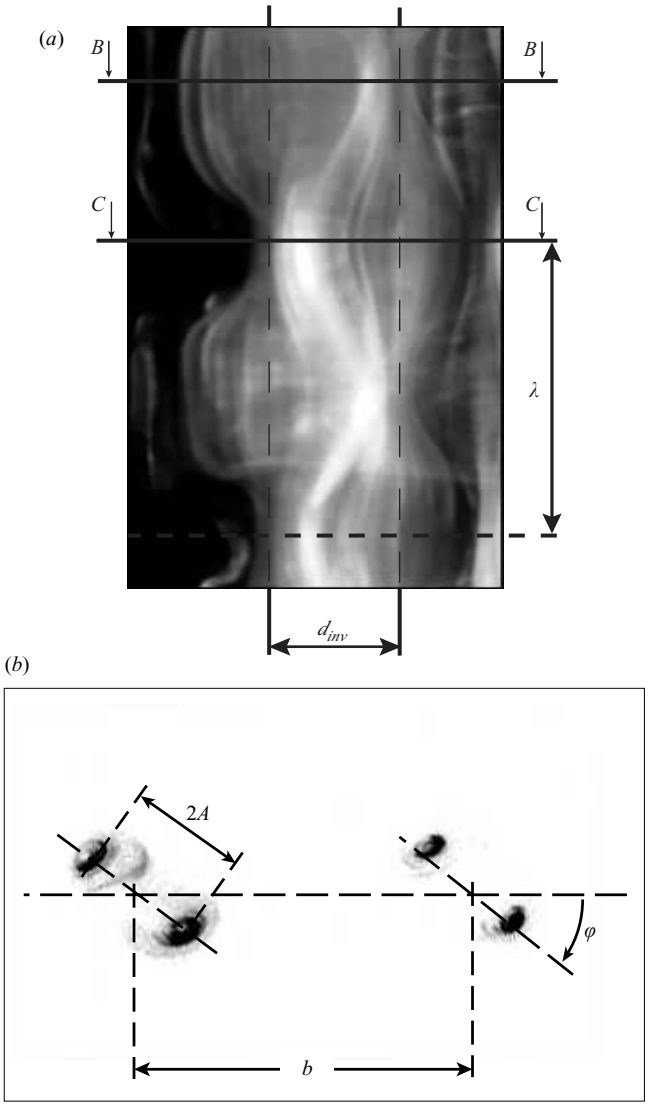


FIGURE 11. (*a*) Close-up view of the three-dimensional instability appearing on one vortex for $Re \approx 3000$ and $\lambda = 3.5$ cm. The invariant stream tube has a diameter d_{inv}. Cross-sections B–B and C–C are separated by half a wavelength. (*b*) Simultaneous visualization, shown as a negative image, of the two sections B–B and C–C, for $Re = 3600$ and $\lambda = 3$ cm. Each vortex shows two centres (corresponding to the two images in sections B–B and C–C), separated by twice the amplitude A of the waviness.

of the instability is observed in a sharp red tip at the inner side of the pair, and a smaller green tip at the outer side of the pair. The two vortex centres have been displaced toward the right and the bottom of the image. The deformation appears very rapidly, i.e. within approximately half a rotation period t_c of the vortex pair.

A close-up side view of the instability found on one vortex is presented in figure 11(*a*). It shows that the instability has a complex radial structure. Around the centreline, there is an invariant stream tube of diameter d_{inv}, which remains cylindrical. Inside this tube the layers of dye are displaced in one direction (to the left on section C–C), whereas they are displaced in the opposite direction (to the right on

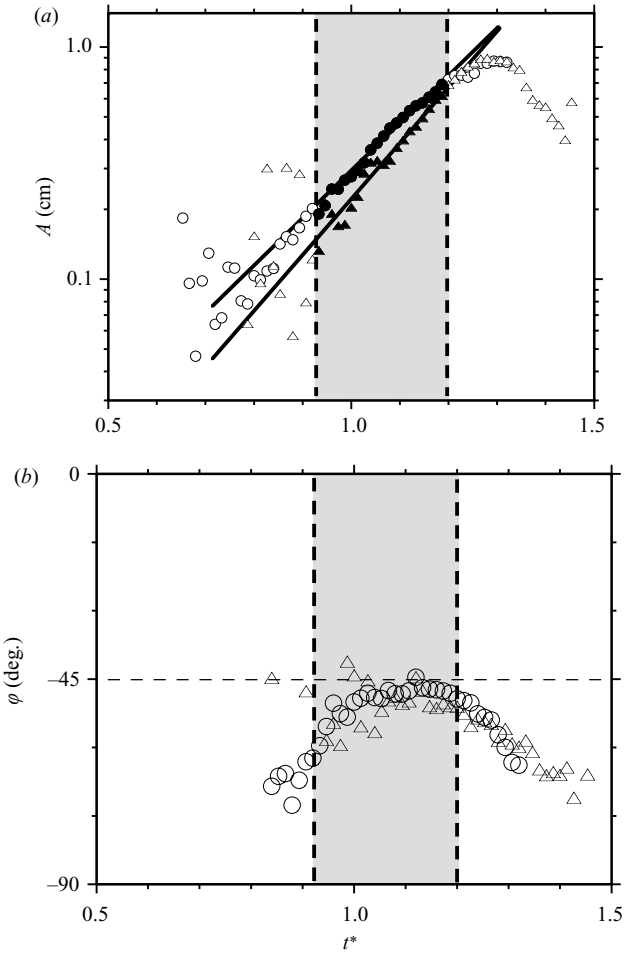


FIGURE 12. (*a*) Amplitude of the vortex centreline perturbation for $Re = 3600$ and $a/b = 0.2$ (this core size is the average value in the shaded time interval). The fit gives growth rates of $\sigma^* = 4.8$ for the first vortex (○) and $\sigma^* = 5.5$ for the second (△). (*b*) Angle φ defined in figure 11(*b*), between the line joining the two vortices and the plane of the perturbation.

section *C*–*C*) outside this tube. Measuring the diameter of this tube gives an average ratio of the diameter d_{inv} and the wavelength λ:

$$\lambda/d_{inv} = 2.3 \pm 0.2. \tag{3.1}$$

The radial velocity of the perturbation must vanish for $r = d_{inv}/2$, so that the dye on this tube is never displaced radially. The value of the diameter of the invariant tube is slightly larger than that found by Leweke & Williamson on a counter-rotating vortex pair ($\lambda/d_{inv} = 2.0 \pm 0.2$), showing that the structure of the instability is close, but not identical to the one observed on a counter-rotating pair.

By simultaneously illuminating the two sections *B*–*B* and *C*–*C* shown on figure 11(*a*), we obtain an image as in figure 11(*b*). Since the sections *B*–*B* and *C*–*C* are located at a maximum and a minimum of the undulations of the centrelines, each vortex centre has two images. The distance between the two centres is twice the amplitude *A* of the undulations. The angle φ gives the orientation of the planes containing the perturbations. This angle is fairly constant in time, whereas the amplitude grows exponentially (see figure 12), as was also shown in Meunier &

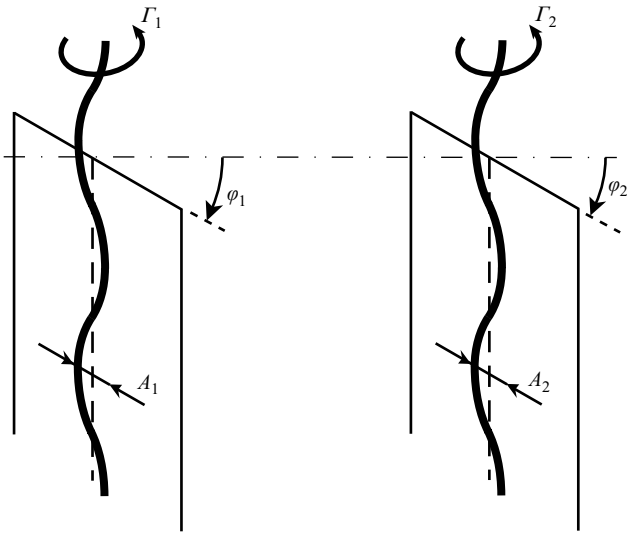


FIGURE 13. Schematic of the three-dimensional structure of the instability.

Leweke (2001). The average angle of the vortices is given by:

$$\varphi = -50^\circ \pm 5^\circ. \tag{3.2}$$

It can be noted that the orientation φ of the planes is negative, if the pair rotates counterclockwise, i.e. when the circulations are positive.

To conclude, the structure of this instability is very well described by the sketch in figure 13 with angles $\varphi_1 = \varphi_2 = -50^\circ$, plus an invariant tube around each vortex, whose diameter is given by (3.1).

4. Comparison with elliptic instability theory

In this section, we demonstrate that the instability observed on the co-rotating vortex pair is a consequence of an elliptic instability of each vortex. We compare the theoretical predictions of growth rate and wavelength with their experimental measurements.

4.1. *Spatial structure*

Each vortex is located in the velocity field induced by the opposite vortex. To order zero, this velocity field is a translation of the first vortex at the velocity $\Gamma/2\pi b$. Since the induction is symmetric, the two vortices move on a circular trajectory of radius $b/2$, with a rotation period given by (2.5). However, each vortex is located in a flow which is locally irrotational and not in solid-body rotation. We now study the flow in the frame of reference centred on one vortex, i.e. in the translated frame that follows the vortex centre. To first order, the velocity field induced by the opposite vortex is a potential stagnation-point flow with a strain rate given by:

$$\varepsilon_{ext} = \Gamma/2\pi b^2. \tag{4.1}$$

The stretching axes are oriented at -45° with respect to the line joining the two vortices. Each vortex is thus located in a stagnation-point flow whose axes rotate at the angular velocity Ω defined by (2.4). Le Dizès (2000*a*) showed that a Gaussian vortex placed in a rotating external stagnation-point flow develops an internal strain

rate ε_{int} at its centre, which depends on the rotation frequency Ω of the external strain. A fit of the ratio of the inner and outer strain is given by Le Dizès & Laporte (2002):

$$\varepsilon_{int}/\varepsilon_{ext} = 1.5 + 0.038\ (0.16 - \Omega/2\mu)^{-9/5}\,, \tag{4.2}$$

where $\mu = \Gamma/2\pi a^2$ is the angular velocity of the fluid at the centre of each vortex. In our symmetric case, the ratio can be simplified into:

$$\varepsilon_{int}/\varepsilon_{ext} = 1.5 + 0.038\,[0.16 - (a/b)^2]^{-9/5}. \tag{4.3}$$

The flow at the centre of the vortex can thus be written as a superposition of solid-body rotation at angular velocity μ and a strain field of strength ε_{int}, rotating at the angular velocity Ω. In the frame rotating at Ω, i.e. with the axes of the external strain, the two-dimensional flow close to the vortex centre $\boldsymbol{U}$ is approximately equal to:

$$\boldsymbol{U} = \begin{pmatrix} 0 & -\widetilde{\mu} - \varepsilon_{int} & 0 \\ \widetilde{\mu} - \varepsilon_{int} & 0 & 0 \\ 0 & 0 & 0 \end{pmatrix} \begin{pmatrix} x \\ y \\ z \end{pmatrix}. \tag{4.4}$$

Here, x and y are the coordinates in the vortex cross-section, with the x-direction being parallel to the line between the vortex centres; the z-axis is given by the unperturbed vortex axis. $\widetilde{\mu} = \mu - \Omega$ is the angular velocity at the centre of the vortex in the rotating frame. We thus have to study the instabilities of such a flow in a frame rotating at the angular frequency Ω. The flow in (4.4) is an exact solution of the Navier–Stokes equation, and its streamlines are ellipses with aspect ratio $E = [(\widetilde{\mu} + \varepsilon_{int})/(\widetilde{\mu} - \varepsilon_{int})]^{1/2}$. Bayly (1986) found a class of perturbations:

$$\boldsymbol{u} = \boldsymbol{v}(t)\exp[\mathrm{i}\boldsymbol{k}(t)\boldsymbol{r}], \tag{4.5}$$

where the amplitude $\boldsymbol{v}$ and the wavevector $\boldsymbol{k}$ are both functions of time. If the superposition $\boldsymbol{U} + \boldsymbol{u}$ is also a solution of the Navier–Stokes equation, the wave vector must satisfy:

$$\boldsymbol{k}(t) = k_0[\sin\xi\cos\upsilon(t - t_0),\ E\sin\xi\sin\upsilon(t - t_0),\ \cos\xi], \tag{4.6}$$

where $\upsilon = (\widetilde{\mu}^2 - \varepsilon_{int}^2)^{1/2}$ is the frequency of precession of the wave vector around the z-axis with a fixed angle ξ, which can vary from 0° to 90°. The scale k_0 is arbitrary in an unbounded domain, but will be determined in § 4.3 through boundary conditions given by the radial size of the vortices. The Navier–Stokes equation fixes the evolution of the amplitude $\boldsymbol{v}(t)$ of the mode, and Bayly (1986) showed, for the case without rotation ($\Omega = 0$), that there exists a band of angles ξ, located around $\xi = 60°$, for which the amplitude $\boldsymbol{v}$ grows exponentially. Further details on the growth rate will be given in § 4.2. For the case with rotation, Le Dizès (2000*b*) showed that the angle ξ of maximum growth increases slightly with Ω:

$$\cos\xi = \frac{\mu - \Omega}{2\mu} = \tfrac{1}{2} - (a/b)^2\,. \tag{4.7}$$

Waleffe (1990) showed that solutions with a given k_0 and ξ could be combined (by integration over t_0) to give disturbances that are localized near the axis of rotation. For vanishing strain, these solutions take a simple analytical form in the cylindrical components (r, φ, z):

$$u_r = \frac{C}{2\tan\xi}\mathrm{e}^{\sigma t}\,[3J_0(k_z\tan\xi r) + J_2(k_z\tan\xi r)]\cos(k_z z)\sin\left(\varphi + \tfrac{1}{4}\pi\right), \tag{4.8}$$

$$u_\varphi = \frac{C}{2\tan\xi} e^{\sigma t} \left[3J_0(k_z \tan\xi r) - J_2(k_z \tan\xi r)\right] \cos(k_z z) \cos\left(\varphi + \tfrac{1}{4}\pi\right), \tag{4.9}$$

$$u_z = C e^{\sigma t} J_1(k_z \tan\xi r) \sin(k_z z) \sin\left(\varphi + \tfrac{1}{4}\pi\right). \tag{4.10}$$

Here, $k_z = k_0 \cos\xi$ is the vertical component of the wave vector $\boldsymbol{k}_0$, and is directly linked to the axial wavelength by $\lambda = 2\pi/k_z$. J_i are Bessel functions of the first kind and C is a constant. These formulae have been given by Waleffe (1990) for $\xi = 60°$, and have been generalized here for $\xi \neq 60°$.

This analysis (leading to the global theory of the elliptic instability) is based on the use of Kelvin waves $\boldsymbol{u}_n(\boldsymbol{r})\exp(\mathrm{i}(k_z z + m\theta - \varpi_n t))$, which are a family of orthogonal solutions of the Navier–Stokes equation, linearized around the two-dimensional vortex. Here, k_z, m and ϖ_n are the axial and azimuthal wavenumbers, and the rotation rate of the spatial mode $\boldsymbol{u}_n(\boldsymbol{r})$, respectively. The shape of the vorticity distribution of the vortex leads to a dispersion relation $\mathrm{D}(k_z, m, \varpi_n) = 0$, which can be found for example in Saffman (1992) for a vortex with uniform vorticity. For each azimuthal wavenumber m, there is an infinity of solution branches $\varpi_n(k)$, numbered by n, which defines the profile $\boldsymbol{u}_n(\boldsymbol{r})$. A strain field of strength ε_{int} has a radial velocity given by:

$$u_r = \varepsilon_{int}\, r\, \cos[2(\varphi + \pi/4)] \propto \varepsilon_{int}\, r\, e^{\mathrm{i}2\varphi}, \tag{4.11}$$

and can be considered as a degenerated Kelvin wave $(k_z = 0, m = 2, \varpi_n = 0)$. Consequently, a triadic resonance may exist (through the nonlinear term of the Navier–Stokes equations) between two Kelvin waves and a strain if the resonance condition,

$$(k_{z,1},\ m_1,\ \varpi_{n,1}) - (k_{z,2},\ m_2,\ \varpi_{n,2}) = (0, 2, 0), \tag{4.12}$$

is satisfied. The two Kelvin waves must have the same k_z and ϖ_n: so, in the $(k_z,\ \varpi_n)$ plane, it corresponds to the intersection of a branch $m = m_1$ with a branch $m = m_2 = m_1 \pm 2$ (usually $m_1 = +1$ and $m_2 = -1$). For this case, Eloy & Le Dizès (2001) showed that the growth rate is always positive, and that it is maximum for reciprocal branches (having the same n). In the co-rotating configuration, the strain rotates at the angular velocity Ω of the vortex pair (defined in § 2.2). The straining field, whose radial velocity is given by:

$$u_r = \varepsilon_{int}\, r\, \cos\left[2(\varphi - \Omega t)\right] \propto \varepsilon_{int}\, r\, e^{\mathrm{i}(2\varphi - 2\Omega t)}, \tag{4.13}$$

is thus equivalent to a Kelvin wave $(k_z = 0, m = 2, \varpi_n = 2\Omega)$. The resonance condition is then:

$$(k_{z,1},\ m_1,\ \varpi_{n,1}) - (k_{z,2},\ m_2,\ \varpi_{n,2}) = (0, 2, 2\Omega). \tag{4.14}$$

This condition is satisfied for $m_1 = +1$, $m_2 = -1$ and $\varpi_1 = \Omega$, $\varpi_2 = -\Omega$. This is why we still expect a three-dimensional elliptic instability at small wavelength in our configuration, whereas the long-wavelength Crow instability is cancelled by the rotation of the vortex pair, as mentioned above. A study of the dispersion relation of the Kelvin waves shows that (4.14) is satisfied for smaller wavenumbers than for the case of a non-rotating strain, which is in good agreement with the experimental evidence. A more detailed study of the observed wavelengths will be carried out in § 4.3.

Leweke & Williamson (1998) showed that this perturbation, added to the flow of a vortex, implies a sinusoidal undulation of the vortex centreline, in a plane oriented at $-45°$. This is exactly what has been observed and described in § 3, except that the angle

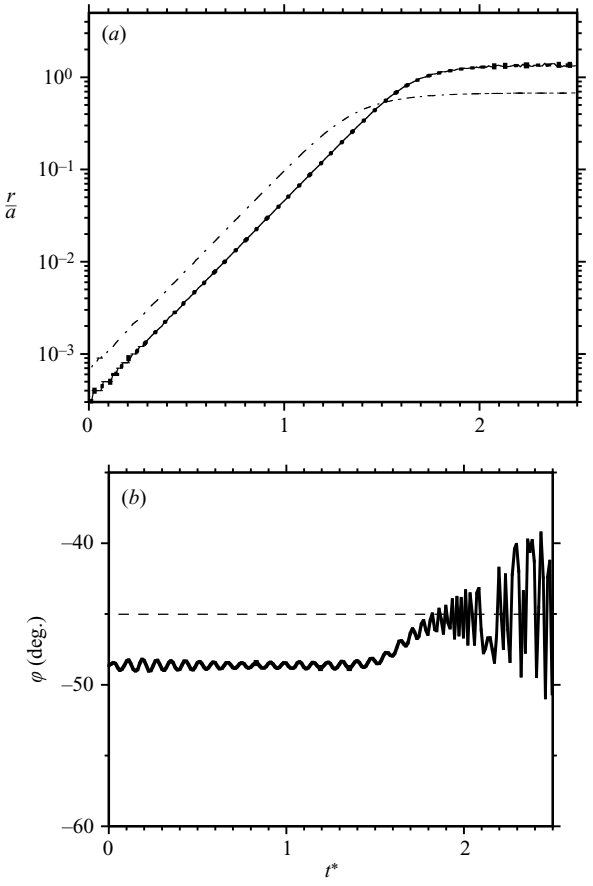


FIGURE 14. Numerical simulation of the trajectory of a dye spot (solid line), initially at the centre of a Gaussian vortex defined by (2.2), which is then superposed with the mode of the elliptic instability (4.8)–(4.10), with a growth rate $\sigma^* = 5$, $a/b = 0.2$, $\lambda = 4a$. (*a*) Radial position r of the dye (with respects to the centre of the Gaussian vortex), compared to the locations of the centre of rotation of the total flow (dashed line) and of the maximum of vorticity (dash-dotted line). (*b*) Angle with a direction corresponding to the line joining the two vortices of a pair.

was closer to $-50°$. This difference is an effect linked to the visualization method: the positions of the dye spots in figure 11(*b*) are not exactly equal to the positions of the centres of rotation since they move as the perturbation grows. Numerical simulation of the Lagrangian trajectory of a dye spot in the flow of a Gaussian vortex (2.2), modified by the three-dimensional perturbation (equations (4.8)–(4.10)) is shown in figure 14. It indicates that the angle of the dye spots is closer to $-50°$ for the typical values of growth rate found in the experiment. Figure 14(*a*) shows that the exponential growth of the amplitude of the dye undulation is exactly equal to the growth rate, provided that it is smaller than the core size a of the vortex, which validates the growth rate measurements using dye visualizations.

Owing to the shape of the Bessel functions, the radial component of the velocity, u_r, vanishes for $k_r r = 2.7346$. This indicates that on a circle of diameter $d_{inv} = 2 \cdot 2.7346/k_r$ the fluid and the dye are not displaced radially. Assuming the angle ξ is $62.42°$, which is obtained for a typical value of $a/b = 0.2$ with (4.7), we obtain a theoretical prediction

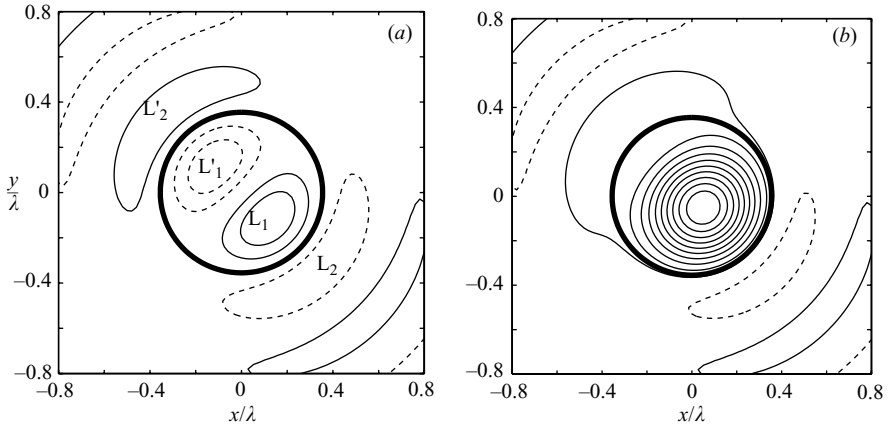


FIGURE 15. (*a*) Theoretical prediction of the axial vorticity found for the elliptic mode defined by (4.16). (*b*) Superposition of this mode with a Gaussian vortex, whose core size equals: $a = \lambda/4$. The perturbation amplitude C equals half the maximum of the vorticity of the Gaussian vortex. The bold line represents the circle where the perturbation vorticity vanishes.

for the ratio between the wavelength and the diameter of the invariant tube:

$$\lambda/d_{inv} = \frac{\pi \tan \xi}{2.7346} = 2.1995. \tag{4.15}$$

This is slightly larger than in the absence of rotation ($\xi = 60^\circ$), where Leweke & Williamson (1998) showed that $\lambda/d_{inv} = 1.9898$. This result is in very good agreement with the experimental value given in (3.1), and explains why the experimental values tend to increase in the presence of rotation (the experimental value found by Leweke & Williamson (1998) was approximately 2).

Waleffe (1990) gave the vertical component of the vorticity perturbation:

$$\omega_z = -2Ck_z \mathrm{e}^{\sigma t} J_1(k_r r) \cos(k_z z) \cos\left(\varphi + \tfrac{1}{4}\pi\right). \tag{4.16}$$

The contours of the axial vorticity are shown in figure 15(*a*). The perturbation vorticity contains two lobes L_1 and L_1' of opposite-signed vorticity inside a circle of diameter $2 \times 3.8325/k_r$. Outside this circle, the vorticity has the opposite sign, which creates two other lobes, L_2 and L_2'. In fact, there is an infinity of lobes of vorticity since the Bessel function $J_1(r)$ of (4.16) oscillates. However, this solution has been found by a local analysis, which is not justified for large r. The study of the Kelvin waves of finite-size vortices (Waleffe 1990) shows that there are two pairs of lobes for the first Kelvin wave ($n = 1$) and three pairs of lobes for the second Kelvin wave ($n = 2$). When adding this perturbation to the flow of a Gaussian vortex defined by (2.2), the resulting peak of vorticity is displaced at -45°, i.e. in the stretching direction of the strain, as shown in figure 15(*b*). The global experimental vorticity field shown in figure 16 indicates that the maximum of vorticity of the two vortices is indeed displaced in the -45° direction. This figure resembles the dye visualization of figure 10(*b*). For a better comparison between the theoretical perturbation vorticity and the experimental results, we must isolate the perturbation from the global vorticity field created by each vortex. We use the fact that the perturbation is antisymmetric with respect to the middle point, since the two perturbations are in phase. The antisymmetric part of the vorticity field

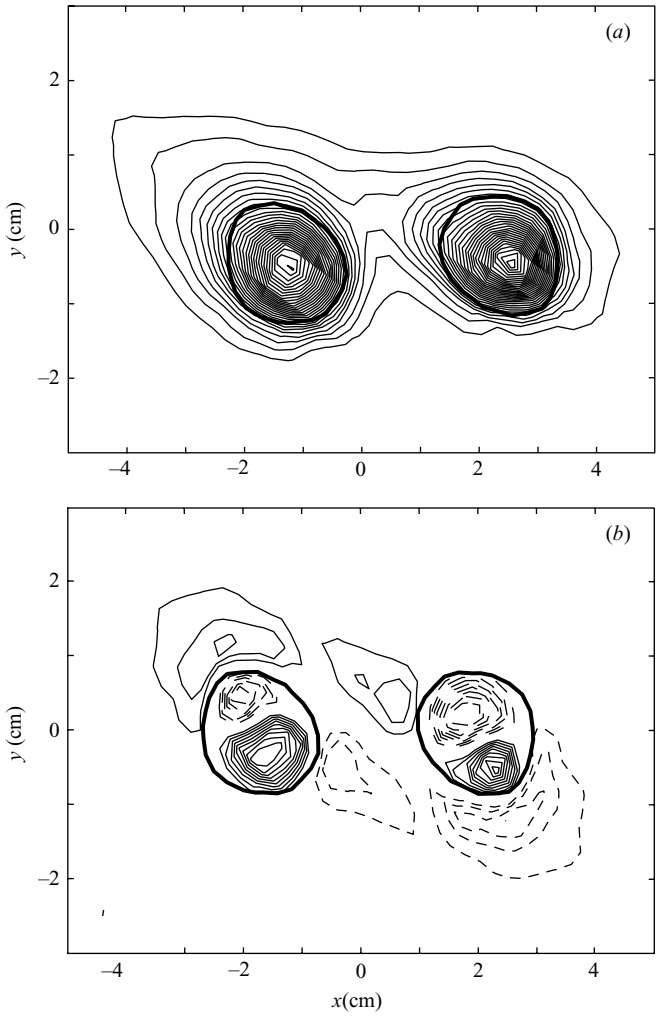


FIGURE 16. Axial vorticity contours of the unstable pair measured experimentally, in a plane located at a maximum of the vortex centre displacement. (*a*) Total flow, (*b*) perturbation. The bold lines represent the tubes where the vorticity of the perturbation vanishes. Dashed contours represent negative vorticity; difference between two vorticity contours is $0.4\,\mathrm{s}^{-1}$. $Re = 3350$, $\lambda = 3.5$ cm.

of figure 16(*a*) corresponds to the perturbation alone, and is shown in figure 16(*b*). For each vortex, it exhibits the features found in figure 15(*a*): two lobes of vorticity of opposite signs exist inside an approximately circular contour, outlined in bold in the figure. The lobes are oriented at $-45°$ with respect to the line joining the vortex centres. Outside each contour, the vorticity changes sign and creates two other lobes of vorticity, as in figure 15(*b*). There are only two pairs of lobes, indicating that it is the first mode of the elliptic instability (linked to the branch of the Kelvin wave with $n = 1$).

4.2. *Growth rate*

Experimentally, the amplitude $A(t)$ is measurable only when it is large enough for the two images of each vortex (see figure 11*b*) to be distinguished. The evolution of $A(t)$

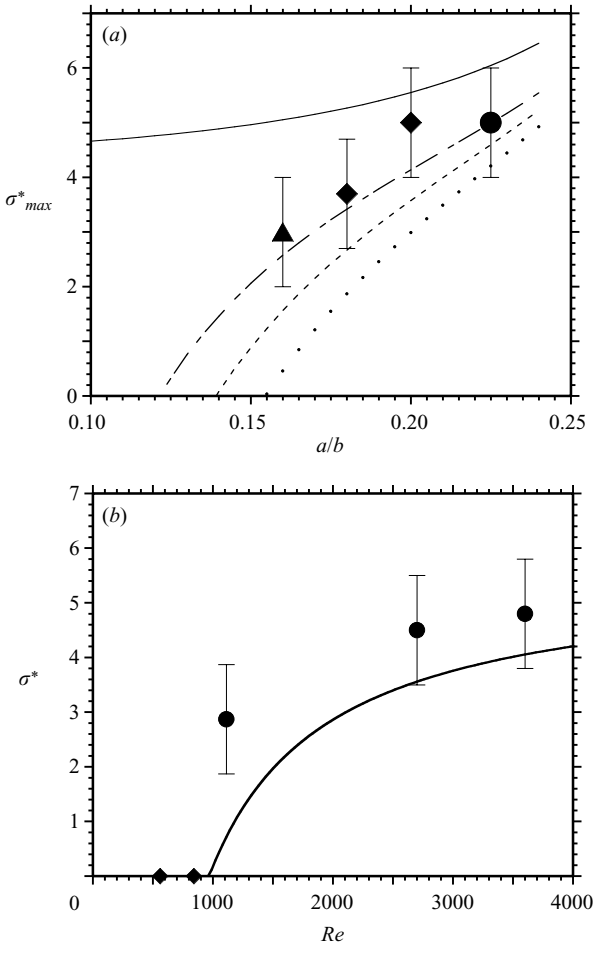


FIGURE 17. Maximum growth rate of the instability obtained experimentally (a) at different ratios a/b (for ▲, $Re = 5000$; ◆, 3600; ●, and 2700 and (b) at different Reynolds numbers (for $\lambda/a = 4$ and $a/b = 0.21$). The lines correspond to theoretical predictions: for infinite Reynolds number (solid line in a) obtained using (4.18), and for $Re = 5000$; (dash-dotted line), $Re = 3600$ (dashed line), and $Re = 2700$ (dotted line) using (4.20).

is shown in figure 12(a); it grows exponentially during a period of 1–2 s. Since a/b increases in time, the choice of a particular a/b, for which we want to determine the growth rate, fixed the time interval in which the amplitude is calculated. The mean separation distance b over this period gives the time t_c used to non-dimensionalize the growth rate. Different wavelengths were excited, and the growth rates were measured by a least-squares fit of the data, in the given period, which was independent of the wavelength. In this way, we were able to measure the maximum growth rate as a function of a/b, which is plotted in figure 17(a). Since the amplitude is only measurable over a decade, the noise is quite large and the uncertainty is found to be approximately 25 %.

It is easy to predict theoretically the value of the maximum growth rate of the instability for infinite Reynolds numbers. Indeed, Kerswell (2002) and Le Dizès &

Laporte (2002) give the maximum growth rate, using the local theory:

$$\sigma_{max} = \left(\frac{3\mu - \Omega}{4\mu}\right)^2 \varepsilon_{int} = \frac{9}{16}\left[1 - \frac{2}{3}\left(\frac{a}{b}\right)^2\right]\varepsilon_{int}. \tag{4.17}$$

Combining this with (2.5), (4.1) and (4.3), we obtain a non-dimensional growth rate:

$$\sigma^*_{max} = \sigma t_c = \frac{9\pi}{16}\left[1 - \frac{2}{3}\left(\frac{a}{b}\right)^2\right]\left[1.5 + 0.038\,(0.16 - (a/b)^2)^{-9/5}\right]. \tag{4.18}$$

However, in our case, the Reynolds number is not infinite, and we must calculate the viscous correction term $\sigma = -\nu k_0^2$ (Landman & Saffman 1987), which depends on the wavelength λ. It is difficult to give an exact formula and we calculated the maximum growth rate by taking the maximum of the growth rate as a function of the wavelength, calculated in § 4.3 using (4.19) and (4.20). We can see in figure 17(*a*) that theory underestimates the growth rates. This may be due to the fact that the merging process slightly increases the growth rates, or that the vorticity profiles of the initial vortices are not exactly Gaussian, which may increase the effective core size a, as mentioned in § 2.2.

Figure 17(*b*) shows that the maximum growth rate decreases for decreasing Reynolds numbers and vanishes for a critical Reynolds number of roughly 1000 (for $a/b = 0.21$). This picture is in very good qualitative agreement with the theory which predicts a critical Reynolds number of 970, although the growth rate is slightly underestimated, as stated above.

4.3. *Wavelength*

The theory outlined in § 4.1 treats the case of an infinite uniform elliptic flow. It is a model of the core region of the vortices. However, the axial wavelength of the instability scales on the radial scale, i.e. on the finite core size a of the vortex. As a consequence, the previous local theory cannot predict the wavelength. Fortunately, the global theory mentioned in § 4.1 can be linked to the preceding theory, since the structure of the mode given by (4.8)–(4.10) corresponds to the analytical expressions of the Kelvin waves in the core of a Rankine vortex, having uniform vorticity in its core and zero vorticity outside. It is thus possible to predict the wavelength λ, using the dispersion relations of the Kelvin waves for a Gaussian vortex. A fit of these dispersion relations can be found in Le Dizès & Laporte (2002). In our configuration, we always observed a stationary perturbation in the rotating frame. This indicates that it is the sum of two Kelvin waves (k_z, $m_1 = +1$, $\varpi_1 = +\Omega$) and (k_z, $m_2 = -1$, $\varpi_2 = -\Omega$). Indeed, this is the only combination able to generate a perturbation $\boldsymbol{u}(r)\exp(\mathrm{i}k_z z)\cos(\theta - \Omega t)$. These Kelvin waves verify the resonance condition (4.14), if they have the same branch number n. They are thus a good candidate for the observed perturbation. For the first branch ($n = 1$), the dispersion relation D(k, m, ϖ) fixes the wavenumber k_z, if one assumes that $\varpi = \Omega$. We thus have a very simple prediction of the wavelength using the resonance condition (4.14) and the dispersion relation of the Kelvin waves.

It is even possible to predict the variation of the growth rate σ as a function of the wavelength, by linking the local and the global theories. This has been done by Le Dizès & Laporte (2002), who found a relation between the angle ξ and the frequency of the Kelvin waves ϖ. Using a fit of the dispersion relation of the Kelvin waves,

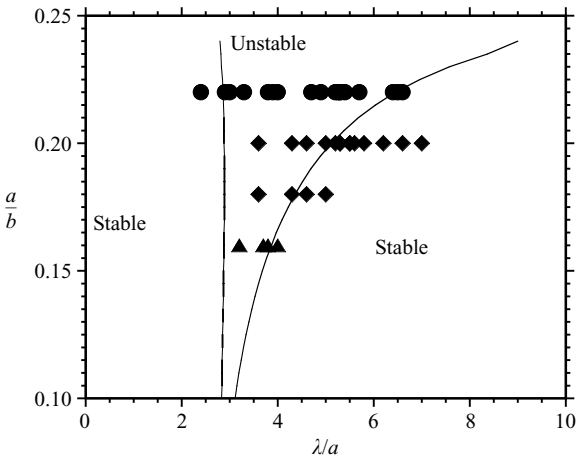


FIGURE 18. Stability diagram for the first mode of the elliptic instability. Symbols represent experimental conditions where exponential growth of the instability was observed. ●, $Re = 2700$; ◆, 3600; ▲, 5000. Lines are obtained for $Re = \infty$ using the theoretical predictions of Le Dizès & Laporte (2001).

they give a link between the angle ξ and the wavenumber, for the first mode of the elliptic instability:

$$\cos\xi = \tfrac{1}{2} - \frac{2.26 - k_z a}{13.9}. \tag{4.19}$$

They also give a global formula for the growth rate as a function of ξ,

$$\sigma = \sqrt{\left(\frac{3\mu - \Omega}{4\mu}\right)^4 \varepsilon_{int}^2 - (\mu - \Omega - 2\mu\cos\xi)^2} - \nu\frac{k_z^2}{\cos^2\xi}, \tag{4.20}$$

in which the viscous effects have been taken into account by adding a viscous damping $-\nu k_0^2$, leading to the second term of the equation. By combining these two equations with (4.3), it is now possible to predict the growth rate of the instability as a function of the wavelength.

The stability diagram including all these results is shown in figure 18. The band of unstable wavelengths becomes very large when a/b grows, since the inner strain ε_{int} becomes very large compared to the external strain because of the rotation of the strain (see (4.3)). This is why the instability band is much larger than for the elliptic instability without rotation. For finite Reynolds numbers, the unstable domain (which is not drawn here) would only appear for high ratios a/b, above a critical ratio $(a/b)_c$ which decreases with the Reynolds number and vanishes at infinite Reynolds numbers. When a/b tends to zero, the unstable band becomes narrower, and is centred around $k_z a = 2.26$, as in the absence of rotation (see Eloy & Le Dizès 1999).

The experimental wavelengths observed for different ratios a/b have been plotted in the stability diagram. The bandwidth of instability indeed increases when a/b increases. The wavelengths are in agreement with the theoretical predictions, but seem slightly larger for $Re = 3600$. This might be because the profiles of vorticity are not exactly Gaussian, and the effective core size might be slightly larger, which would shift the experimental results to the left and to the top, i.e. closer to the theoretical prediction.

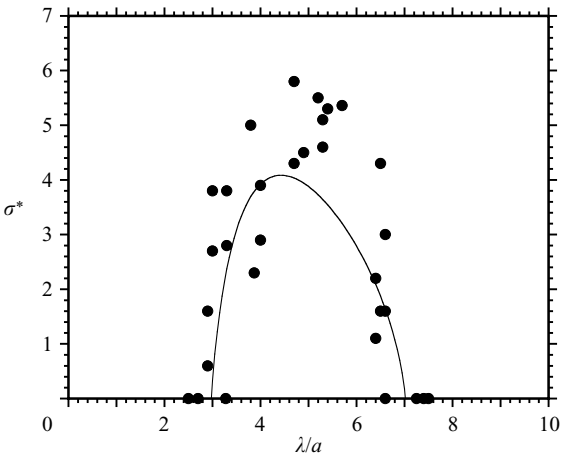


FIGURE 19. Non-dimensional growth rate as function of the wavelength, for $Re = 2700$ and $a/b = 0.22$. The solid line corresponds to the theoretical prediction of Le Dizès & Laporte (2001).

Figure 19 shows the growth rate as a function of the wavelength for a fixed ratio a/b. The experimental results have a large scatter because these types of measurement are very difficult to achieve. For simultaneous measurements of growth rate and wavelength, two cameras have been used to obtain cross-cut and side views at the same time. Moreover, the flow is extremely sensitive to background noise and residual fluid motion in the tank; the experiments were repeated several times, until a clean measurement of $A(t)$ was obtained. This is the first time that a complete growth rate curve is obtained experimentally for the elliptic instability in an open flow configuration, with a surprisingly good agreement with theory. Indeed, the measured growth rate qualitatively follows the theoretical prediction, but appears to be slightly larger, as mentioned in § 4.2. The prediction of the band of unstable wavelengths is excellent which validates all the hypothesis made in the theory.

4.4. *Symmetric mode of the elliptic instability*

We have carried out a systematic study of the elliptic instability, by varying the wavelength λ and the ratio a/b. The ratio a/b at which the instability becomes visible decreases drastically with increasing Reynolds number: for higher Reynolds numbers, a/b increases more slowly and the growth rate is higher. We almost always observed an antisymmetric perturbation of the vortices, except for a very narrow band of the parameters, for which a symmetric perturbation of the vortices would grow (independent of the symmetric or antisymmetric initial excitation). This structure of the elliptic instability is shown in figure 20. It appeared for $a/b = 0.22$ and a non-dimensional wavelength λ/a approximately equal to 3, at a Reynolds number of 3600. For this Reynolds number, the usual antisymmetric perturbation was observed for larger wavelengths $3.5 < \lambda/a < 7.5$. We thus think that this perturbation is linked to the second mode of the elliptic instability, i.e. for the second branch of the Kelvin waves ($n = 2$). However, the growth rate was measured to be

$$\sigma^* = 8.5 \pm 1.5, \tag{4.21}$$

whereas a theoretical prediction made as in § 4.2 gives a maximum value of 1.77 for the growth rate of this mode at $a/b = 0.22$. The discrepancy might come from the

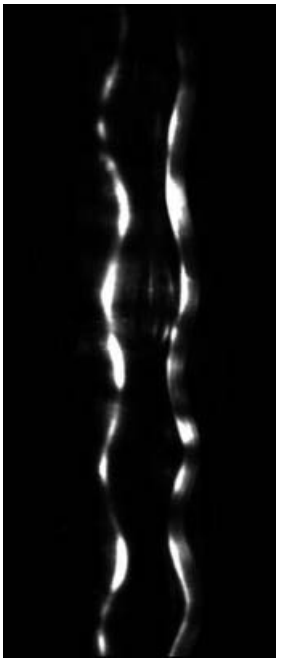


FIGURE 20. Side-view visualization of a symmetric perturbation of the vortices, possibly involving the second radial mode of the elliptic instability. $Re = 3600$; $\lambda/a = 3.4$; $a/b = 0.22$.

effect of the merging, which can possibly lead to a significant acceleration of the growth.

Since the second radial Kelvin mode appears for smaller wavelengths, the viscous decay term $(-\nu k_0^2)$ in the growth rate is larger, and they are less visible for moderate Reynolds numbers. However, this mode has been well observed numerically at high Reynolds numbers using large eddy simulations (Leweke *et al.* 2001). In these simulations, the perturbation is antisymmetric with respect to the middle between the two vortices, unlike what we observed experimentally.

The standard antisymmetric perturbation can be explained by the fact that in this configuration the radial velocity $u_n(r)$ of both vortices must move the fluid in the same direction at the centre of the vortex pair (see Leweke & Williamson 1998). This matching condition is not fulfilled for the symmetric mode if both vortices have the same radial structure ($n = 1$). However, the matching condition can be fulfilled for the symmetric perturbation if one vortex is perturbed with the mode $n = 1$ (with one invariant tube) and the other vortex with the mode $n = 2$ (with two invariant tubes), as shown schematically in figure 21(*a*). The symmetric perturbation can only appear when both modes ($n = 1$ and $n = 2$) of the elliptic instability are unstable in the same band of parameters. Figure 21(*b*) shows that this happens for $\lambda/a \approx 3$, i.e. close to where we found experimentally the symmetric perturbation. The coexistence of the two different radial modes $n = 1$ and $n = 2$ therefore seems a very plausible explanation of the symmetric perturbation of the elliptic instability. It may be noted that in the absence of rotation of the strain, e.g. for counter-rotating vortex pairs, the unstable bands for the different radial modes always remain narrow and never overlap. A symmetric perturbation mode of such a pair is therefore not possible.

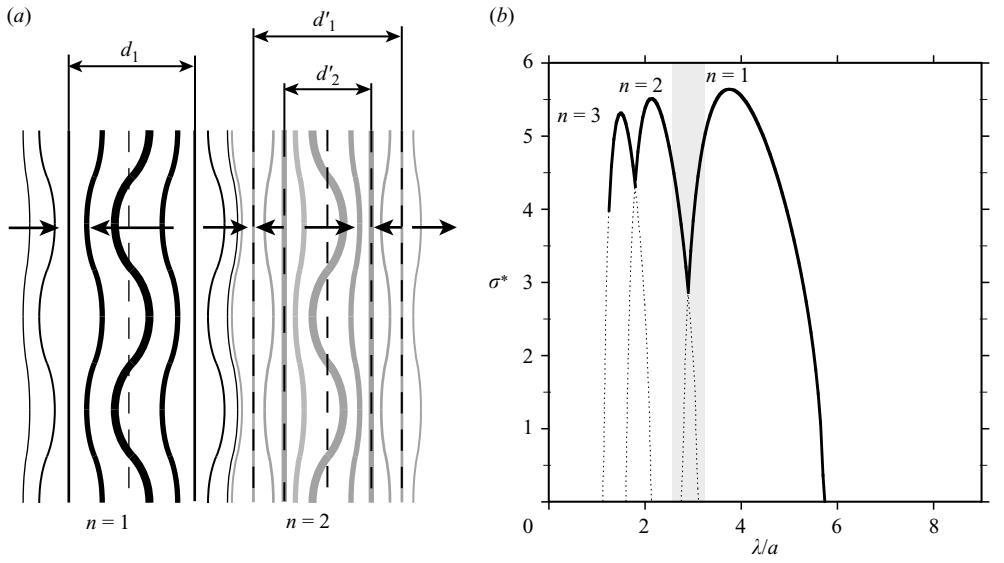


FIGURE 21. (*a*) Sketch of the spatial structure for a symmetric perturbation: the left vortex has one invariant tube (mode $n = 1$) and the right vortex has two invariant tubes (mode $n = 2$). (*b*) Theoretical curves of the growth rate for $\mathrm{Re} = 10^5$ and $a/b = 0.205$ for the first three modes of the elliptic instability. The grey band indicates the region where the first two modes coexist, possibly leading to a symmetric perturbation of the vortices.

5. Late stages and merging

In the two previous sections, we have described in detail the characteristics of the instability in its initial linear stage, for which comparison with theoretical predictions concerning elliptic instability of a single vortex in a rotating strain were possible. In the following, we focus on the later stages of the flow, which are specific to the configuration of a co-rotating vortex pair, and in particular on the effect of the three-dimensional instability on vortex merging.

5.1. *Onset of merging*

When the amplitude of the instability mode becomes sufficiently large, the two vortices merge into a single vortex, just as for the case without elliptic instability. However, in the presence of instability, the beginning of merging, i.e. the start of the decrease of the separation distance b, appears to depend more on the instability amplitude, rather than on the relative core size a/b. Indeed, merging has been observed in this study for a/b as small as 0.19, whereas Meunier *et al.* (2002) found that merging begins only when a/b reaches a critical value of 0.24 in the absence of a three-dimensional instability. This different behaviour can be explained by the fact that, in the presence of the instability, some vorticity is shifted radially away from its initial vortex by the perturbation (see figure 16*a*). It is possible that this vorticity crosses the streamline separating the vortex from the outer flow (see Meunier (2001) and Cerretelli & Williamson (2003) for more details on the merging process), in which case it is carried away into filaments, which are ejected from the vortex pair. Such filaments, which are well known in the two-dimensional case, are visible at the end of the merging stage in figure 22(*a*). For the conservation of the angular momentum, the two vortices must be closer when the filaments are ejected, and merging begins. The

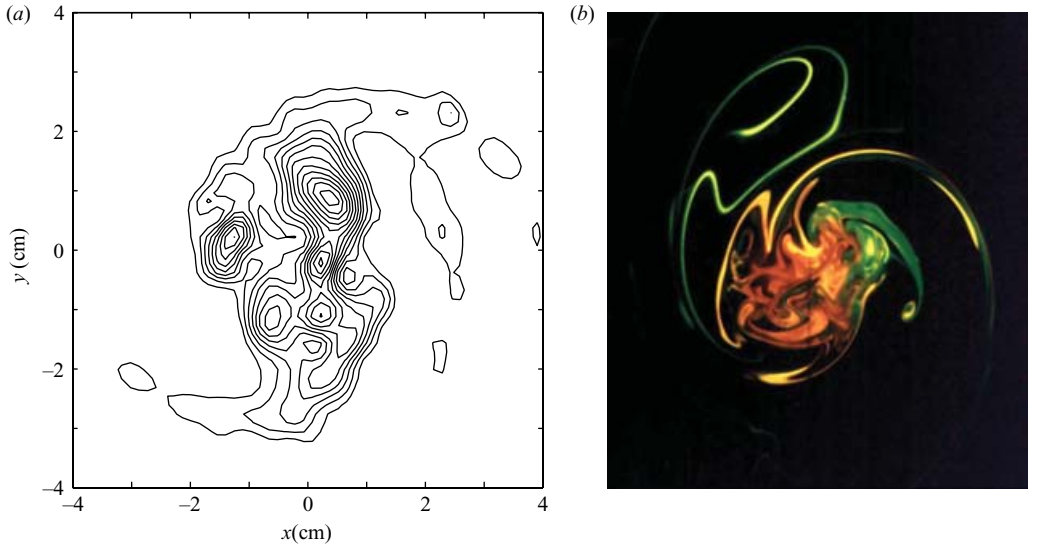


FIGURE 22. Cross-cut view of the turbulent final vortex.(*a*) Vorticity contours at $t^* = 1.6$, for $Re = 3600$ and $\lambda = 4.5$ cm. (*b*) Dye visualization for $t^* \approx 1.6$, $Re \approx 3000$ and $\lambda = 3.5$ cm.

premature creation of these filaments by the instability leads to an earlier merging. Such a nonlinear behaviour has already been observed for quasi-geostrophic vortices by Dritschel & de la Torre Juarez (1996), where a three-dimensional instability allows merger from greater distances.

5.2. *Transient turbulent state*

During and immediately after the merging process, the vorticity field, shown in figure 22(*a*), has a very chaotic structure. This almost turbulent behaviour, involving small-scale structures, is even more visible in the cross-cut dye visualizations in figure 22(*b*) and the side-view in figure 23. In these visualizations, the dye filaments have been stretched and bent in a disorganized way. Moreover, they seem to have smaller radii than the primary vortices. Indeed, the vorticity field of figure 22(*a*) contains five separate vortices of small size, embedded in a large area of disorganized vorticity.

These small structures could be the signature of secondary vortices, which have been stretched by the primary vortices. Indeed, when a thin vorticity tube nears the hyperbolic stagnation point between the two vortices, it can be stretched significantly, so that its radius decreases and its length and vorticity level increase. It is then advected by the global flow and tends to wrap around the vortex pair. Such secondary vortices are clearly visible in figure 24, where the dye tubes are the signature of these transverse secondary structures.

5.3. *Relaminarization of the final vortex*

Once the merging is finished, the final vortex reorganizes into a more symmetric structure, as shown in figure 25. The dye and vorticity structures are stretched and roll up around the final vortex owing to the differential rotation of the global flow.

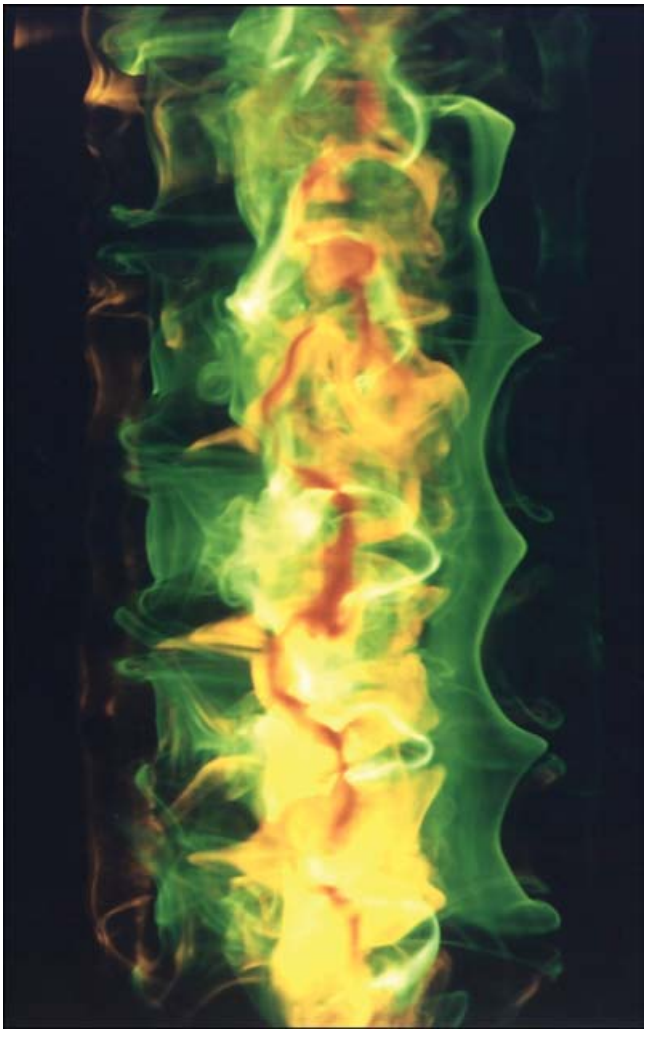


FIGURE 23. Side-view visualization of the turbulent final vortex, after merging of the two vortices in the presence of the elliptic instability for $t^* \approx 1.6$ and $\lambda = 3.5$ cm. $Re \approx 3000$.

This leads to an axisymmetrization of the final vortex, as described by Melander & McWilliams (1987). In the vortex centre, the flow is almost in solid-body rotation, and it takes a longer time for the axisymmetrization process to be effective there. When the vorticity filaments are close enough, the diffusion process smoothes the vorticity into an axisymmetric distribution. It takes longer for the dye pattern to be smoothed since the diffusivity of the dyes is several orders of magnitude lower than the kinematic viscosity of the fluid.

As for two-dimensional flow, the profile of vorticity of the final vortex resulting from the merging is not Gaussian. However, it is still possible to define a core size, using the procedure described in § 2.2, by measuring the radius at which the averaged azimuthal velocity is maximum. The evolution of the square of the core size is shown in figure 26, as a function of the viscous time, and compared to the case of merging without instability. In the latter situation, merging sets in at $a/b \approx 0.24$, and the area



FIGURE 24. Close-up view of the secondary vortices, which are stretched around the final vortex. $Re \approx 3000$ and $\lambda = 3.5$ cm.

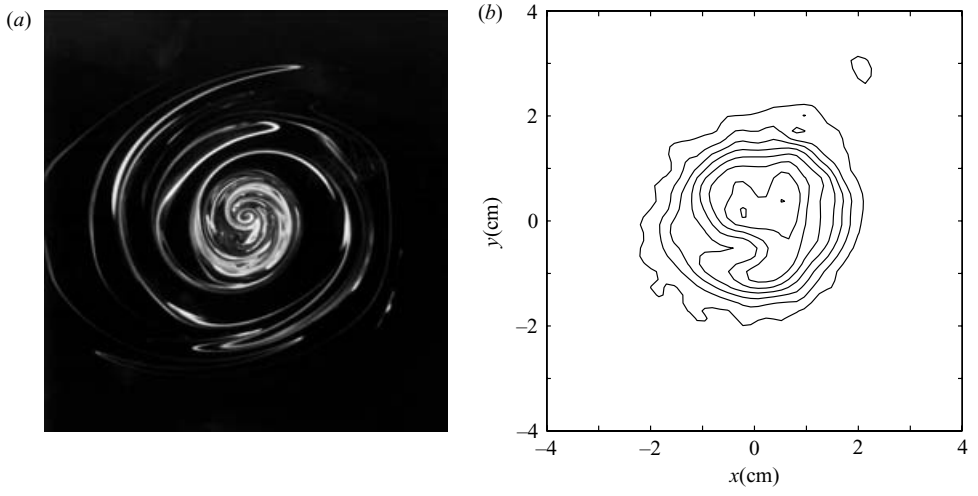


FIGURE 25. Cross-cut view of the final vortex after relaminarization, in the case of merging with the elliptic instability. (*a*) Dye visualization for $t^* \approx 2$, $Re \approx 3000$ and $\lambda = 3.5$ cm. (*b*) Vorticity contours at $t^* = 2.2$, for $Re = 3600$ and $\lambda = 4.5$ cm.

of the final vortex is about twice as large as the one of each initial vortex. In the presence of instability, figure 26 clearly shows that merging starts earlier, i.e. for lower a/b, and that the core area more than triples during this process. The net result, as far as these measurements show, and assuming that the relaminarized vortex area evolves similarly to that of a Gaussian vortex (equation (2.3)), is that the final vortex appears to be larger than it would have been without instability. Such a scenario had already been suggested by Meunier & Leweke (2001), based on a single experiment, and is here confirmed. Owing to the disturbances induced by end effects in our experimental set-up, the evolution of the flow could not be followed long enough to obtain more precise results at these later stages.

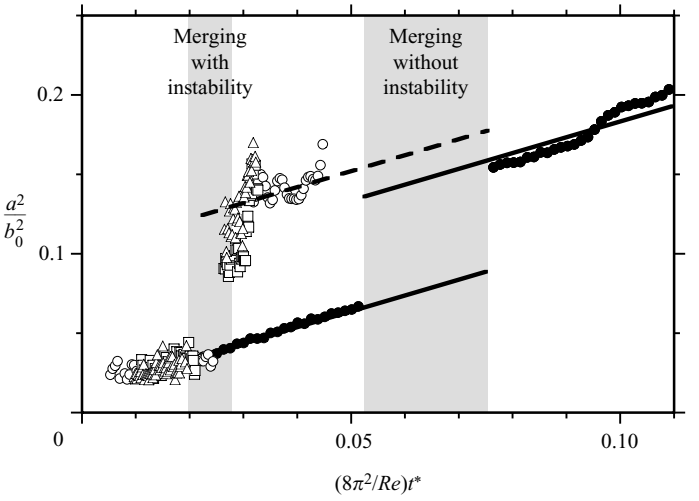


FIGURE 26. Evolution of the square of the non-dimensional core radius a/b, as function of the non-dimensional viscous time. In the presence of the instability (open symbols), merging appears earlier than in the absence of the instability (filled symbols). ●, $Re = 1506$; ○, $Re = 3350$ and $\lambda = 3.5$ cm; □, $Re = 5000$ and $\lambda = 2.3$ cm; △, $Re = 5000$ and $\lambda = 2.7$ cm.

5.4. *Profile of the final vortex*

The characterization of the final vortex through only one parameter (the core size a) is too simplistic, since the profile of vorticity is not Gaussian after merging. Figure 27 shows the velocity and the circulation as a function of the radius. At small and large Reynolds numbers, the profile exhibits an excess of velocity (or circulation) outside the inner core of the final vortex. The velocity profile scales approximately as $v_\varphi \propto r^{-2/3}$, instead of $v_\varphi \propto r^{-1}$ for a Gaussian vortex. This scaling appears to be independent of the type of merging involved (turbulent or laminar).

This excess of velocity is due to the presence of vorticity outside the core, which comes from the filaments of vorticity ejected during the merging process. If the vortices are embedded in an arbitrary two-dimensional outer flow, the filaments could be trapped by neighbouring vortices after their ejection, which would change the size and profile of the merged vortex. The circulation of this vortex would not be twice the circulation of the initial vortex, but less; its profile would probably be closer to Gaussian, and its core would be slightly smaller. This assumption was used by Carnevale *et al.* (1991) to build a theory of two-dimensional turbulence through vortex merging: in their theory the circulation was not conserved during merging, but the energy and the enstrophy were. They calculated a final size of the merged vortex equal to $2^{1/4}$ times the initial size of the vortex, whereas we obtained a final size equal to $\sqrt{2}$ times the initial size, consistent with the conservation of circulation. The role of the filaments of vorticity could provide an explanation for this discrepancy.

6. Conclusion

In this paper, we have presented experimental results concerning the short-wavelength elliptic instability of a pair of co-rotating vortices. This three-dimensional

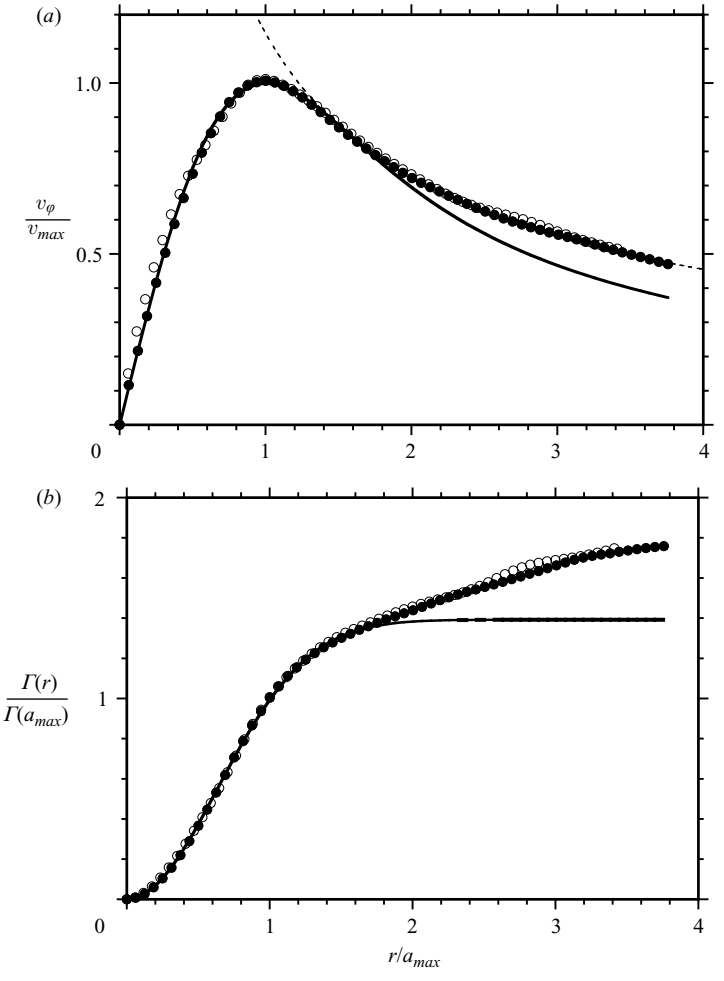


FIGURE 27. Final (*a*) azimuthal velocity and (*b*) local circulation after the merging of the two vortices without instability at $Re = 1506$ (filled symbols) and with instability at $Re = 3350$ (open symbols). The solid line is the prediction for a Gaussian distribution of vorticity for which $v_\varphi \propto r^{-1}$. The dashed line corresponds to a vortex with $v_\varphi \propto r^{-2/3}$.

instability, well studied in a counter-rotating vortex pair, is still present in such a flow, which is characterized by the fact that each vortex experiences a time-dependent rotating external strain. Extensive dye visualizations and measurements using particle image velocimetry allowed us to obtain precise information about the structure and quantitative features of the instability.

The instability consists of three-dimensional internal deformations of the vortex cores, involving a growing waviness of the vortex centrelines and the existence of an invariant streamtube in each core. The perturbation mode is found to be stationary in the frame of reference of the rotating pair and, except for a very narrow range of wavelengths, is antisymmetric with respect to the central point of symmetry of the initial pair. These features are very similar to those of the short-wave instability found by Leweke & Williamson (1998) in a counter-rotating vortex pair. As in their case, the mode structure identifies the instability as an elliptic instability of the vortex cores, which is a general mechanism in strained vortical flows. The symmetry properties can

be understood from the matching condition between the perturbations of the two vortices.

Elliptic instability of a strained vortex can be explained by a resonant interaction between (normally neutral) Kelvin waves of the vortex and the strain. The fact that the strain rotates in the present configuration, has a number of consequences for the quantitative instability characteristics. First, the resonance occurs for larger wavelengths as for the non-rotating case, which is confirmed by our measurements. Secondly, the growth rates are higher, which can be understood by an increased internal strain rate at the vortex centre, owing to a modified adaptation of the flow to the rotating external strain (Le Dizès 2000*a*). The most striking feature, however, is the dramatic increase of the width of the unstable wavelength interval with increasing rescaled core size a/b, which characterizes the effect of the rotation of the pair, as revealed for the first time by the present measurements.

The experimental stability diagram as a function of wavelength and core size, as well as different measurements of the instability wavelength, as a function of Reynolds number, core size and wavelength, were compared to theoretical predictions by Le Dizès & Laporte (2002), based on the analysis of a single vortex in a rotating strain. The overall agreement was found to be very good.

The fact that the unstable wavelength bands of the elliptic instability widen considerably with increasing rotation, may lead to an overlap of different bands, associated with different types of bending modes. This may be related to the observation of a symmetric three-dimensional perturbation for certain parameters. In fact, this mode appeared at the inferior limit of the unstable wavelength interval of the principal mode, at a location, where, in the case of overlapping bands, the second radial mode could also have a positive growth rate. The presence of this second mode in one vortex and the principal one in the other would lead again to a kinematic matching of the perturbations between the vortices, whereas the centrelines would be deformed symmetrically. This is the first time that evidence of the second radial mode of elliptic instability has been detected experimentally in a freely developing strained vortex.

In the late stages of the flow, the perturbations induced by the instability, combined with the specific flow field of the co-rotating vortex pair, lead to the periodic generation and ejection of vorticity filaments. This, in turn, makes the primary cores approach each other, thus initiating the merging process. Owing to the strong three-dimensional perturbations, this 'unstable' merging leads to a sudden breakdown of the organized structure into small-scale turbulent motion. Visualizations have shown how secondary transverse vortices are generated in this process, which subsequently are wrapped around the outer part of the merging vortex. Measurements reveal that the merging process begins earlier, i.e. for smaller core sizes than for the well-known case of two-dimensional flow, and that the final vortex, which in our low-Reynolds-number flow rapidly relaminarizes, appears to have a larger radius than for stable merging.

The authors wish to thank S. Le Dizès for many helpful discussions during the course of this study. This work was supported by the European Commission under Contract no. G4RD-CT-1999-00141 (C-Wake).

REFERENCES

Bayly, B. J. 1986 Three-dimensional instability of elliptical flow. *Phys. Rev. Lett.* **57**, 2160–2163.

Bayly, B. J., Orszag, S. A. & Herbert, T. 1988 Instability mechanisms in shear-flow transition. *Annu. Rev. Fluid Mech.* **20**, 359–391.

Cadot, O., Douady, S. & Couder, Y. 1995 Characterization of the low-pressure filaments in a three-dimensional turbulent shear flow. *Phys. Fluids* **7**, 630–646.

Carnevale, G. F., McWilliams, J. C., Pomeau, Y., Weiss, J. B. & Young, W. R. 1991 Evolution of vortex statistics in two-dimensional turbulence. *Phys. Rev. Lett.* **66**, 2735–2737.

Cerretelli, C. & Williamson, C. H. K. 2003 The physical mechanism for vortex merging. *J. Fluid Mech.* **475**, 41–77.

Chen, A. L., Jacob, J. D. & Savas, Ö. 1999 Dynamics of corotating vortex pairs in the wakes of flapped airfoils. *J. Fluid Mech.* **378**, 155–193.

Craik, A. D. D. 1989 The stability of unbounded two- and three-dimensional flows subject to body forces: some exact solutions. *J. Fluid Mech.* **198**, 275–292.

Craik, A. D. D. & Criminale, W. O. 1986 Evolution of wavelike disturbances in shear flow: a class of exact solutions of the Navier–Stokes equations. *Proc. R. Soc. Lond.* A **406**, 275–292.

Crow, S. C. 1970 Stability theory for a pair of trailing vortices. *AIAA J.* **8**, 2172–2179.

Devenport, W. J., Vogel, C. M. & Zsoldos, J. S. 1999 Flow structure produced by the interaction and merger of a pair of co-rotating wing-tip vortices. *J. Fluid Mech.* **394**, 357–377.

Dritschel, D. G. 1985 The stability and energetics of corotating uniform vortices. *J. Fluid Mech.* **157**, 95–134.

Dritschel, D. G. 1986 The nonlinear evolution of rotating configurations of uniform vortices. *J. Fluid Mech.* **172**, 157–182.

Dritschel, D. G. & de la Torre Juarez, M. 1996 The instability and breakdown of tall columnar vortices in a quasi-geostrophic fluid. *J. Fluid Mech.* **328**, 129–160.

Eloy, C. & Le Dizès, S. 1999 Three-dimensional instability of Burgers and Lamb-Oseen vortices in a strain field. *J. Fluid Mech.* **378**, 145–166.

Eloy, C. & Le Dizès, S. 2001 Stability of the Ramkine vortex in a multipolar strain field. *Phys. Fluids* **13**, 660–676.

Eloy, C., Le Gal, P. & Le Dizès, S. 2000 Experimental study of the multipolar instability. *Phys. Rev. Lett.* **85**, 3400–3403.

Fabre, D. & Jacquin, L. 2004 Short-wave cooperative instabilities in representative aircraft vortices. *Phys. Fluids* **16**, 2142.

Greenspan, H. P. 1968 *The Theory of Rotating Fluids*. Cambridge University Press.

Griffiths, R. W. & Hopfinger, E. J. 1987 Coalescing of geostrophic vortices. *J. Fluid Mech.* **178**, 73–97.

Jiménez, J. 1975 Stability of a pair of co-rotating vortices. *Phys. Fluids* **18**, 1580–1581.

Kerswell, R. R. 2002 Elliptical instability. *Annu. Rev. Fluid Mech.* **34**, 83–113.

Kida, S. & Ohkitani, K. 1992 Spatiotemporal intermittency and instability of a forced turbulence. *Phys Fluids* A **4**, 1018–1027.

Krutzsch, C.-H. 1939 Über eine experimentell beobachtete Erscheinung an Wirbelringen bei ihrer translatorischen Bewegung in wirklichen Flüssigkeiten. *Ann. Phys.* **35**, 497–523.

Landman, M. J. & Saffman, P. G. 1987 The three-dimensional instability of strained vortices in a viscous fluid. *Phys. Fluids* **30**, 2339–2342.

Le Dizès, S. 2000*a* Non-axisymmetric vortices in two-dimensional flows. *J. Fluid Mech.* **406**, 175–198.

Le Dizès, S. 2000*b* Three-dimensional instability of a multipolar vortex in a rotating flow. *Phys. Fluids* **12**, 2762.

Le Dizès, S. & Laporte, F. 2002 Theoretical predictions for the elliptic instability in a two-vortex flow. *J. Fluid Mech.* **471**, 169–201.

Leblanc, S. 1997 Stability of stagnation points in rotating flows. *Phys. Fluids* **9**, 3566–3569.

Leblanc, S. & Cambon, C. 1998 Effects of the Coriolis force on the stability of Stuart vortices. *J. Fluid Mech.* **356**, 353–379.

Leweke, T., Meunier, P., Laporte, F. & Darracq, D. 2001 Controlled interaction of co-rotating vortices. In *3rd ONERA-DLR Aerospace Symp. (ODAS 2001)* (ed. K. Bütefisch *et al.*), Paper S2-3.

Leweke, T. & Williamson, C. H. K. 1998 Cooperative elliptic instability of a vortex pair. *J. Fluid Mech.* **360**, 85–119.

Lifschitz, A. & Hameiri, E. 1991 Local stability conditions. *Phys. Fluids* A **3**, 2644–2651.

Malkus, W. V. R. 1989 An experimental study of global instabilities due to tidal (elliptical) distortion of a rotating elastic cylinder. *Astrophys. Fluid Dyn.* **48**, 123–134.

MAXWORTHY, T. 1972 The structure and stability of vortex rings. *J. Fluid Mech.* **51**, 15–32.

MELANDER, M. V. & MCWILLIAMS, J. C. 1987 Axisymmetrization and vorticity-gradient intensification of an isolated two-dimensional vortex through filamentation. *J. Fluid Mech.* **178**, 137–159.

MELANDER, M. V., ZABUSKY, N. J. & MCWILLIAMS, M. J. 1988 Symmetric vortex merger in two dimensions: causes and conditions. *J. Fluid Mech.* **195**, 303–340.

MEUNIER, P. 2001 Etude expérimentale de deux tourbillons corotatifs. PhD thesis, Université de Provence Aix-Marseille I, Marseille, France.

MEUNIER, P., EHRENSTEIN, U., LEWEKE, T. & ROSSI, M. 2002 A merging criterion for two-dimensional co-rotating vortices. *Phys. Fluids* **14**, 2757–2766.

MEUNIER, P. & LEWEKE, T. 2000 Unstable vortex merger. *Phys. Fluids* **12**, S6, Gallery of Fluid Motion.

MEUNIER, P. & LEWEKE, T. 2001 Three-dimensional instability during vortex merging. *Phys. Fluids* **13**, 2747–2751.

MEUNIER, P. & LEWEKE, T. 2003 Analysis and treatment of errors caused by high velocity gradients in PIV. *Exps Fluids* **35**, 408–421.

MOORE, D. W. & SAFFMAN, P. G. 1975*b* The instability of a straight filament in a strain field. *Proc. R. Soc. Lond.* A. **346**, 413–425.

OVERMAN, E. A. & ZABUSKY, N. J. 1982 Evolution and merger of isolated vortex structures. *Phys. Fluids* **25**, 1297–1305.

PIERREHUMBERT, R. T. 1986 Universal short-wave instability of two-dimensional eddies in an inviscid fluid. *Phys. Rev. Lett.* **57**, 2157–2159.

ROBERTS, K. V. & CHRISTIANSEN, J. P. 1972 Topics in computational fluid mechanics. *Comput. Phys. Comm. (suppl.)* **3**, 14–32.

SAFFMAN, P. & SZETO, R. 1980 Equilibrium of a pair of equal uniform vortices. *Phys. Fluids* **23**, 2339–2342.

SAFFMAN, P. G. 1992 *Vortex Dynamics*. Cambridge University Press.

THOMAS, P. J. & AUERBACH, D. 1994 The observation of the simultaneous development of a long- and a short-wave instability mode on a vortex pair. *J. Fluid Mech.* **265**, 289–302.

TSAI, C.-Y. & WIDNALL, S. E. 1976 The stability of short waves on a straight vortex filament in a weak externally imposed strain field. *J. Fluid Mech.* **73**, 721–733.

VINCENT, A. & MENEGUZZI, M. 1991 The spatial structure and statistical properties of homogeneous turbulence. *J. Fluid Mech.* **225**, 1–20.

VLADIMIROV, V. A., MAKARENKO, V. G. & TARASOV, V. F. 1987 Experimental investigation of non-axisymmetric inertia waves in a rotating fluid. *Fluid Dyn.* **22**, 151.

WALEFFE, F. 1990 On the three-dimensional instability of strained vortices. *Phys. Fluids* A **2**, 76.

WIDNALL, S. E. & SULLIVAN, J. P. 1973 On the stability of vortex rings. *Proc. R. Soc. Lond.* A **332**, 335–353.